Unsteady radiative heat transfer model of a ceria particle suspension undergoing solar thermochemical reduction

Roman Bader[1]
The Australian National University, Canberra, ACT 2601, Australia

Lukas Gampp[2]
ETH Zurich, CH-8092, Switzerland

Tristan Breuillé[3]
École Polytechnique Fédérale de Lausanne, CH-1015, Switzerland

Sophia Haussener[4]
École Polytechnique Fédérale de Lausanne, CH-1015, Switzerland

Aldo Steinfeld[5]
ETH Zurich, CH-8092, Switzerland

and
Wojciech Lipiński[6]
The Australian National University, Canberra, ACT 2601, Australia
E-mail: wojciech.lipinski@anu.edu.au

Unsteady radiative heat transfer is analyzed numerically in a directly-irradiated plane-parallel medium containing a suspension of ceria particles undergoing non-stoichiometric thermal reduction. The micrometer-sized ceria particles are assumed to be homogenous, non-gray, absorbing, emitting, and anisotropically scattering, while the overall medium is of non-uniform temperature and composition. The unsteady mass and energy conservation equations are solved using the finite-volume method and the Shampine–Gordon time integration scheme. Radiative transport is modeled using the energy-portioning Monte Carlo ray-tracing method with radiative properties obtained from the Mie theory. Increasing particle volume fraction and decreasing particle diameter both increase the optical thickness of the particle suspension, resulting in increasing peak temperature and non-stoichiometry at steady state. For 5 μm-dia. particles under 1000 suns irradiation, the peak temperature at steady state

---

[1] Research Fellow, Research School of Engineering.
[2] Master Student, Department of Mechanical and Process Engineering.
[3] Master Student, School of Engineering.
[4] Assistant Professor, School of Engineering.
[5] Professor, Department of Mechanical and Process Engineering.
[6] Professor, Research School of Engineering, AIAA senior member.

ranges from 1855 K for a particle volume fraction of $f_\mathrm{v} = 10^{-6}$ to 2092 K for $f_\mathrm{v} = 10^{-4}$; the temperature non-uniformity ranges from 9 to 622 K. For a fixed volume fraction of $f_\mathrm{v} = 10^{-6}$, decreasing the particle diameter from 20 to 1 μm increases the peak temperature at steady state from 1734 to 2162 K; the temperature non-uniformity increases from 9 to 61 K.

Nomenclature

A = area, m^2

a_p = specific surface area of particles, m^{-1}

Bi = Biot number

C = solar concentration ratio

$\bar{c}_p$ = specific heat capacity, $\mathrm{J\ kmol^{-1}\ K^{-1}}$

d = diameter, m

E = emissive power, $\mathrm{W\ m^{-2}}$

f_v = volume fraction

G_b = direct normal solar irradiance, $\mathrm{W\ m^{-2}}$

h = enthalpy, $\mathrm{J\ kg^{-1}}$

$\bar{h}$ = molar enthalpy, $\mathrm{J\ kmol^{-1}}$

h_conv = convective heat transfer coefficient, $\mathrm{W\ m^{-2}\ K}$

$\bar{h}_\mathrm{f}$ = molar enthalpy of formation, $\mathrm{J\ kmol^{-1}}$

I = radiative intensity, $\mathrm{W\ m^{-2} sr^{-1}}$

i = index

j = control volume index

k = absorptive index

L = thickness of infinite slab, m

M = molar weight, $\mathrm{kg\ kmol^{-1}}$

m = complex refractive index

$\dot{m}''_{\mathrm{sf}}$ = interfacial mass flux, $\mathrm{kg\,m^{-2}\,s^{-2}}$

n = refractive index; time step index

$\dot{n}''_{\mathrm{sf}}$ = kinetic rate constant, $\mathrm{kmol\ m^{-2}\ s^{-1}}$

$\mathrm{Nu_p}$ = Nusselt number

p = pressure, Pa

$p_{\mathrm{O_2}}$ = oxygen partial pressure, Pa

Q = efficiency factor

$\dot{q}$ = heat rate, W

$\dot{q}''$ = heat flux, $\mathrm{W\ m^{-2}}$

$\dot{q}'''$ = volumetric heat source, $\mathrm{W\ m^{-3}}$

$\bar{R}$ = universal gas constant, $\mathrm{J\ kmol^{-1}\ K^{-1}}$

$\Re$ = random number

r = radius, m

$\dot{r}'''_{\mathrm{O_2}}$ = oxygen release rate, $\mathrm{kg\,m^{-3}\,s^{-1}}$

$\mathrm{Re_p}$ = Reynolds number

s = geometric path length, m

$\hat{\mathbf{s}}$ = direction unit vector

T = temperature, K

t = time, s

t^* = dummy variable, s

u_{g} = gas flow velocity, $\mathrm{ms^{-1}}$

V = volume, $\mathrm{m^3}$

x = particle size parameter

x, y, z = Cartesian coordinates

Greek Letters

β = extinction coefficient, $\mathrm{m^{-1}}$

$\Delta\bar{h}^{\mathrm{o}}_{\mathrm{O_2}}$ = standard oxidation enthalpy, $\mathrm{J\ kmol^{-1}}$

$\Delta\bar{h}_{\mathrm{red}}$ = molar enthalpy of reduction reaction, $\mathrm{J\ kmol^{-1}}$

$\Delta\bar{s}^{\mathrm{o}}_{\mathrm{O_2}}$ = standard oxidation entropy, $\mathrm{J\ kmol^{-1}\ K^{-1}}$

Δz = layer thickness, m

$\Delta\delta$ = change in non-stoichiometry

$\Delta\tau$ = time interval, s

δ = non-stoichiometry

ε = emissivity

Φ = scattering phase function

φ = azimuthal angle, rad

κ = absorption coefficient, $\mathrm{m^{-1}}$

λ = wavelength, nm

θ = polar angle, rad

ρ = density, $\mathrm{kg\ m^{-3}}$

σ = Stefan–Boltzmann constant, $\mathrm{W\ m^{-2} K^{-4}}$

σ_{s} = scattering coefficient, $\mathrm{m^{-1}}$

Ω = solid angle, sr

ω = scattering albedo

Subscripts

0 = initial value

a = absorbed

ave = average

b = blackbody

cv = control volume

e = emission

i = incident

i,j = indices

ox = oxidation

P = Planck-mean

p = particle

rad = radiative

red = reduction

ref = reference state

s = scattered

surr = surrroundings

x, y = stoichiometric coefficients

λ = spectral

Other symbols

$\langle \; \rangle$ = superficial average

$\langle \; \rangle^{g}$ = intrinsic average over the gas phase

$\langle \; \rangle^{s}$ = intrinsic average over the solid phase

I. Introduction

SOLAR thermochemical splitting of H_2O and CO_2 into synthesis gas (syngas, H_2 + CO), followed by Fischer–Tropsch synthesis, is a promising route to produce CO_2-neutral jet fuel. Splitting H_2O/CO_2 via two-step metal oxide redox cycles offers the potential to achieve high energy conversion efficiencies and avoids the high temperatures and the need for high-temperature gas separation involved with the direct thermolysis of H_2O/CO_2 [1]–[3] (e.g. 20% dissociation would require temperatures of around 2600 to 2800 K [4]). In non-stoichiometric two-step metal oxide redox cycles, a metal oxide is first partially reduced by exposure to concentrated solar radiation according to:

$$\frac{1}{\Delta\delta}\mathrm{M}_x\mathrm{O}_{y-\delta_{\mathrm{ox}}} \rightarrow \frac{1}{\Delta\delta}\mathrm{M}_x\mathrm{O}_{y-\delta_{\mathrm{red}}} + \frac{1}{2}\mathrm{O}_2 \qquad (1)$$

In reaction (1), $\Delta\delta = \delta_{\mathrm{red}} - \delta_{\mathrm{ox}} > 0$ is the change in oxygen non-stoichiometry in the metal oxide, where δ_{ox} is the non-stoichiometry in the oxidized state and δ_{red} is that in the reduced state. In this process step, oxygen is driven out of the metal oxide lattice via mixed electronic/ionic conduction of charge carriers, while the crystal structure itself remains unchanged. In the second process step, the reducing power of the partially or fully reduced metal oxide is utilized to split H_2O and CO_2 according to:

$$\frac{1}{\Delta\delta}\mathrm{M}_x\mathrm{O}_{y-\delta_{\mathrm{red}}} + \mathrm{H_2O} \rightarrow \frac{1}{\Delta\delta}\mathrm{M}_x\mathrm{O}_{y-\delta_{\mathrm{ox}}} + \mathrm{H_2} \tag{2a}$$

$$\frac{1}{\Delta\delta}\mathrm{M}_x\mathrm{O}_{y-\delta_{\mathrm{red}}} + \mathrm{CO_2} \rightarrow \frac{1}{\Delta\delta}\mathrm{M}_x\mathrm{O}_{y-\delta_{\mathrm{ox}}} + \mathrm{CO} \tag{2b}$$

Thereby, oxygen is reintroduced into the oxygen vacancies of the crystal lattice. Metal oxide materials that have been considered for this process include undoped [5],[6] and doped ceria [7]–[9], and several perovskite-type mixed metal oxides [10]–[12]. Ceria is a promising candidate due to its potential to reach oxygen non-stoichiometries of up to δ_{red} = 0.25 without undergoing a phase change, thus maintaining its high oxygen conductivity and avoiding the need for a separation process to recover the metal oxide from the product gas mixture [6],[13],[14].

Several solar reactor designs have been proposed to implement thermochemical redox cycles to split H_2O/CO_2, using either solid porous metal oxide structures or metal oxide particles. Agrafiotis et al. [15], Roeb et al. [16], Chueh et al. [17], Furler et al. [18], and Furler et al. [19] developed and tested cylindrical cavity receiver-reactors containing stationary reactive material structures to conduct the two process steps sequentially and at different temperatures in a single reactor. Kaneko et al. [20] and Diver et al. [21] developed rotary-type reactors in which the reactive material structure alternately rotates through a sunlit reduction zone and a cooler fuel production zone. The latter reactor design implements solid-solid heat recuperation between the two process steps to increase the process efficiency [22],[23]. A similar reactor concept was studied by Lapp & Lipiński [24].

In addition, several particle-based reactors have been developed and tested. Haueter et al. [25], Müller et al. [26], Schunk et al. [27], Schunk et al. [28], and Villasmil et al. [29] developed, tested, and upscaled a rotating cylindrical cavity receiver-reactor to conduct the dissociation of ZnO particles. The particles are fed into the reactor with a screw feeder and line the reactor walls by the centrifugal effect. The particles are directly exposed to concentrated solar radiation and an inert gas flow, to dissociate them into Zn(g) and O_2(g). Gokon et al. [30] conducted the solar thermal reduction of ferrite particles in an internally circulating fluidized bed reactor. Perkins et al. [31] conducted the dissociation of ZnO particles in an electrically heated aerosol flow reactor with particles entrained in inert gas. Koepf et al. [32] developed and tested an upward facing cavity receiver-reactor for the dissociation of ZnO particles. The particles are fed onto the conical cavity wall, where they are exposed to concentrated solar radiation, and are moved by gravity towards the central exit at the bottom of the reactor. Dissociated Zn(g) and aerosolized small particles are entrained and removed through the reactor's exit by an inert vortex gas flow inside the cavity. Weiss et al. [33], Wegner et al. [34], Ernst et al. [35], Hamed et al. [36], Melchior et al. [37], and Loutzenhiser et al. [38] used hot-wall aerosol reactors for the in-situ formation of Zn nanoparticles followed by their oxidation with steam or CO_2. Funke et al. [39] also used an aerosol flow tube reactor to study this reaction. Loutzenhiser et al. [40] and Stamatiou et al. [41] conducted the oxidation reaction with H_2O/CO_2 in an electrically heated packed bed reactor containing a mixture of ZnO and Zn particles. The reactor proposed by Ermanoski et al. [42] consists of two separate reaction chambers. In the reduction reactor, ceria particles are moved through a vacuum chamber with a screw elevator that additionally serves as a solid-solid heat recuperator and a gas sealing, while the fuel production step occurs off-sun and at ambient pressure. Recently, Scheffe et al. [43] developed and tested an aerosol flow reactor consisting of an electrically heated alumina tube containing falling ceria particles in a counter flow with inert sweep gas.

Particle-flow reactors have also been used for other solar thermochemical processes, including the carbothermal reduction of metal oxides [44], the steam gasification of carbonaceous feedstock, including coal [45],[46], petcoke [47], biochar [48],[49], and biomass [50], CO_2 capturing from ambient air via carbonation/calcination cycling [51], co-production of syngas and lime by combined $CaCO_3$-calcination and CH_4-reforming [52], and manganese oxide reduction [53].

The use of metal oxide particles to conduct the process (1)–(2) offers several advantages, including: *i*) volumetric radiation absorption by the particle bed directly at the reaction site, which minimizes heat transfer limitations and irreversibilities due to high temperature gradients in case of indirect heat transfer via conduction through a diathermal wall; *ii*) high specific surface area at the particle/gas interface, which leads to high heat and mass transfer between the phases; *iii*) small length scale of the solids, which minimizes temperature and concentration gradients inside the solid phase, and *iv*) relative ease of manufacture and mechanical stability of particles. Using particles in an aerosol flow reactor additionally offers the benefits of: *i*) a high degree of mixing of the solid and gas, leading to uniform temperature and material distributions in the reactor, *ii*) minimizing the risk of agglomeration and sintering of the particles, and *iii*) relatively simple process control and handling of the particles.

The use of active particles in the reactor introduces new parameters that need to be understood and optimized in the reactor design in order to optimize the reactor performance. These parameters include the particle size, volume fraction and residence time, the gas flow rate and velocity, characteristic particle bed dimensions, incident solar radiative flux, and more. An accurate heat and mass transfer model of the reactor is a useful tool to make informed decisions on the reactor design parameters. In particular, this requires the appropriate modeling of radiative heat transfer inside the reactor. In the present study, transient radiative heat transfer is analyzed numerically in a directly irradiated suspension of ceria particles undergoing thermal reduction, Eq. (1). The model domain chosen for this study is an infinite slab filled with a homogenous suspension of micrometer-sized ceria particles that are directly and perpendicularly irradiated with concentrated solar radiation, and surrounded by non-participating (cold) walls. The particles are assumed to be subjected to a fluidizing gas flow with flow velocity equal to the minimum fluidization velocity and to remain suspended, stratified and exposed to the incident radiation until they reach a steady state, as opposed to real reactors, where particles are subject to higher flow rates, turbulent mixing and a residence time distribution and typically exit the reactor before complete conversion has been reached. In terms of non-uniformity of temperatures and reaction extents in the reactor, the current flow situation constitutes a “worst case” situation with minimal heat and mass exchange by advection and turbulent mixing. The results provide insights to the importance of good mixing conditions in an actual reactor.

The generic model system studied here minimizes the complexity of the modeled domain and allows for the focused and systematic study of the interaction of radiation with the particles undergoing the reduction reaction. For example, the influence of parameters such as particle size and volume fraction on radiative heat transfer and particle heat-up rate can be studied in isolation, without the added complexities of the particle/gas flow pattern and turbulent mixing encountered in an actual reactor, particle residence time distribution, and radiative heat exchange with hot participating surroundings. An actual solar reactor model guiding the design process should couple combined heat transfer including spectral radiative transfer to chemical kinetics in a three-dimensional solution space with realistic boundary conditions, and employ accurate thermophysical properties of the reacting and non-reacting materials. To reduce the model complexity and thus the computational cost, approximations can be employed, in particular for spectral radiative transfer in three-dimensional highly-scattering participating media. Examples of previous pertinent studies can be found in [26, 28, 54–60].

This simplified model system, while not immediately representative of an actual solar chemical reactor, provides valuable insights to the intrinsic heat and mass transfer physics and allow for order-of-magnitude estimates of several important parameters involved in the design of a new reactor. These parameters include particle size, volume fraction, bed thickness and residence time, and irradiation flux density. The simulation results provide insights to particle heating rates, reaction rates and reaction extents, and temperature uniformity in the bed. These insights will be of value for the first-stage design of a particle-based solar reactor to conduct the ceria reduction reaction.

The present study elucidates current limitations to the accurate modeling of radiative transfer in a suspension of reacting ceria particles. These include uncertainty in the available data for the optical properties of ceria and lack of optical properties for non-stoichiometric ceria, which offer opportunities for further research. Finally, the model provides the basis for the development of more complex, multi-dimensional models representative of actual solar reactors or portions thereof and for further numerical analysis of additional parameters not studied in this paper. To our knowledge, this is the first report of a detailed numerical model of radiative heat transfer in a bed of suspended ceria particles undergoing thermochemical reduction under direct solar irradiation.

Previous work has investigated heat and mass transfer in packed- and fluidized-beds of directly irradiated particles for various other solar thermochemical processes. Lipiński & Steinfeld [61] simulated the transient heat transfer in a packed-bed of $CaCO_3$ particles undergoing calcination under direct solar irradiation. Schunk et al. [28] modeled the transient heat transfer in a directly irradiated shrinking packed-bed of ZnO particles undergoing thermal dissociation. The transient radiative heat transfer in directly irradiated particle suspensions has been simulated by Lipiński & Steinfeld [62] and Lipiński et al. [63] for coal particles undergoing steam gasification and by Lipiński et al. [64] for ZnO particles undergoing thermal dissociation. Von Zedtwitz & Steinfeld [45], von Zedtwitz et al. [46], Z'Graggen & Steinfeld [65], and Z'Graggen & Steinfeld [66] went on to simulate heat and mass transfer in actual fluidized bed and vortex flow reactors hosting the steam gasification of carbonaceous particles. Müller et al. [26], Schunk et al. [67], and Villasmil et al. [29] simulated transient heat transfer in the rotating cylindrical cavity receiver-reactor lined with ZnO particles described in Refs.[25]–[29]. Heat transfer in tubular aerosol flow reactors was modeled by Perkins & Weimer [68], Haussener et al. [69], and Melchior et al. [70] for the thermal dissociation of ZnO, and by Melchior et al. [48] and Martinek et al. [71] for the steam gasification of bio char and coal char. Moreover, in recent years particle-based thermal and thermochemical redox systems according to process (1)–(2) have gained increasing interest for high-temperature solar energy storage [72]–[75].

II. Problem statement

The model system is shown schematically in Fig. 1. It consists of a suspension of micrometer-sized cerium dioxide particles that are fluidized in a flow of nitrogen sweep gas with initial oxygen content of 10 ppm. The particle suspension is modeled as a 1-D infinite slab, with infinite extent in *x* and *y* directions and thickness L in *z*-direction. This renders the model system a 1-D problem, with properties (temperature, oxygen partial pressure, and non-stoichiometry) varying only along *z*-direction. The slab contains randomly arranged particles, which are surrounded by black plane boundaries at 0 K (non-participating surroundings). This isolates the model system from its surroundings in terms of heat exchange, to avoid the complexities involved with radiative heat exchange in an enclosure. This is not a thermally optimized configuration. In practice the reactor will need to be contained in an enclosure to reduce radiative heat losses.

The gas flow is assumed to be in *x*-direction with flow velocity equivalent to the minimum fluidization velocity. This means that the particles are suspended by the flow but are not entrained in the flow and hence remain stationary. While this corresponds to lower gas flow velocities than those encountered in actual reactors, this allows studying the entire reduction reaction of the particles without the limitation of finite residence times in actual fluidized bed reactors. Boundary effects on the flow at the impermeable walls at $z=0$ and $z=L$ are omitted from consideration, i.e. the gas is assumed to have a uniform velocity profile along *z*-direction.

The particle cloud is directly exposed to concentrated solar radiation at *z* = 0. The incident solar radiation is assumed to have the spectral distribution of a blackbody at 5780 K. Due to the high temperatures reached by the particles and the low oxygen content in the sweep gas, the ceria particles undergo partial thermal reduction according to Eq. (1), thereby releasing oxygen into the gas phase. The process considered in this study involves ceria particles that undergo a relatively small change in their oxygen content without change in their phase and without significant change in their size and density. Hence, for radiative transfer calculations, the particles can be assumed to be homogenous (0% porosity) and monodisperse, and the particle size and volume fraction can be assumed constant over time. Particles are further treated as isothermal (Bi<<1), spherical, and independently scattering.

Transient heating simulations of a dense ceria particle with the largest diameter studied in this paper ($20\ \mu\text{m}$) were conducted to verify the assumption of isothermal particles. The particle, initially at room temperature and ambient pressure, was subjected to a step change in temperature at the surface from 300 to 1773 K—approximately the steady-state temperature of the suspension reached in this study. Surface temperature was held constant and heat transfer by conduction into the particle was calculated numerically. The particle reached a uniform temperature distribution along its radius within less than 20 ms. This time scale is at least 2 orders of magnitude shorter than the duration of the heat-up simulations studied here. This confirms that the particles can be assumed to be isothermal for the purpose of studying heat transfer in the particle suspension.

The particle suspension is further modeled as uniform, non-gray, absorbing, emitting, anisotropically scattering, and isothermal within a control volume. The gas phase is assumed to be radiatively non-participating, while convective heat transfer and oxygen mass transfer between particles and gas are non-negligible and are taken into account. Hence, as oxygen is released by the particles, the oxygen concentration in the gas phase increases.

The ideal gas assumption is used. The total pressure, p, is assumed uniform and constant throughout the infinite slab. Conduction and diffusion are neglected in both phases. Two cases are considered for the spatial discretization of the model domain. One, the case where particles are assumed to be stratified in the z-direction. This case is modeled by dividing the model domain in multiple layers along the z-axis direction with no particle movement between layers. Two, the case where particles are allowed to move freely in z-direction. This case is modeled with a single layer in z-direction, assuming the particles to mix ideally within the modeling domain. The Monte Carlo ray-tracing method and the Mie theory are used to model the radiative heat transfer in the suspension. The kinetic rate expression for the underlying chemical reaction is adopted from Keene et al. [76].

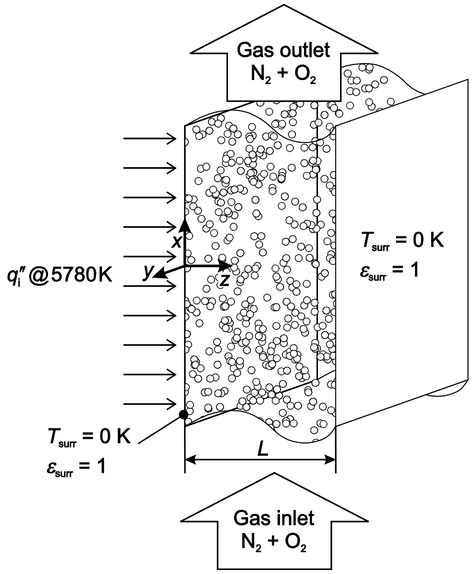

Fig. 1 Schematic of the model system.

III. Governing equations

In this section, the governing transient volume-averaged mass and energy conservation equations, including the boundary and initial conditions, are formulated for both the suspended solid ceria particles and the gas phase. In addition, the radiative transfer equation is formulated and the Nu-correlation for particle-gas convective heat transfer is specified.

A. Mass conservation

The volume-averaged mass conservation equation for the solid phase is given by [76]:

$$\frac{\partial \langle \rho_{\mathrm{p}}(t) \rangle}{\partial t} = -\langle \dot{r}'''_{\mathrm{O}_2}(t) \rangle \tag{3}$$

where $\langle \ \rangle$ denotes the superficial volume average and $\dot{r}'''_{\mathrm{O}_2}$ is the rate of oxygen transfer between solid and gas phase, given in section IV. The volume-averaged density of the solid phase is given by:

$$\langle \rho_{\mathrm{p}}(t) \rangle = f_{\mathrm{v}} \langle \rho_{\mathrm{p}}(t) \rangle^{\mathrm{s}} \tag{4}$$

where $\langle \rho_{\mathrm{p}} \rangle^{\mathrm{s}}$ is the density of the solid phase, averaged over the volume of the solid phase, which can be expressed as a function of the non-stoichiometry $\langle \delta \rangle^{\mathrm{s}}$ and the density of stoichiometric ceria, ρ_{CeO_2} :

$$\langle \rho_{\mathrm{p}}(t) \rangle^{\mathrm{s}} = \rho_{\mathrm{CeO}_2} \left(1 - \frac{1}{2} \frac{M_{\mathrm{O}_2} \langle \delta(t) \rangle^{\mathrm{s}}}{M_{\mathrm{CeO}_2}} \right) \tag{5}$$

Since the oxygen partial pressure and temperature of the gas phase are uniform along *x* and *y*, the oxygen partial pressure in the gas phase can be calculated from:

$$\langle p_{\mathrm{O}_2}(t) \rangle^{\mathrm{g}} = \langle p_{\mathrm{O}_2,0} \rangle^{\mathrm{g}} + \frac{\bar{R} \langle T_{\mathrm{g}}(t) \rangle^{\mathrm{g}}}{M_{\mathrm{O}_2}} \int_0^t \langle \dot{r}'''_{\mathrm{O}_2}(t^*) \rangle \mathrm{d}t^* \tag{6}$$

B. Energy conservation

The volume-averaged energy conservation equation for the solid phase reduces to [76]:

$$f_\mathrm{v}\frac{\partial}{\partial t}\left(\left\langle\rho_\mathrm{p}\right\rangle^\mathrm{s}\left\langle h_\mathrm{p}\right\rangle^\mathrm{s}\right)=\left\langle\dot{q}'''_{\mathrm{O}_2}\right\rangle-\left\langle\dot{q}'''_\mathrm{conv}\right\rangle-\left\langle\nabla\cdot\dot{\mathbf{q}}''_\mathrm{rad}\right\rangle \tag{7}$$

Simplifying the left-hand side using $\frac{\partial}{\partial t}\left(\left\langle h_\mathrm{p}\right\rangle^\mathrm{s}\right)\approx c_{p,\mathrm{p}}\frac{\partial}{\partial t}\left(\left\langle T_\mathrm{p}\right\rangle^\mathrm{s}\right)$ and Eqs. (3)–(4) yields:

$$f_\mathrm{v}\frac{\partial}{\partial t}\left(\left\langle\rho_\mathrm{p}\right\rangle^\mathrm{s}\left\langle h_\mathrm{p}\right\rangle^\mathrm{s}\right)=f_\mathrm{v}\left\langle\rho_\mathrm{p}\right\rangle^\mathrm{s}c_{p,\mathrm{p}}\frac{\partial}{\partial t}\left(\left\langle T_\mathrm{p}\right\rangle^\mathrm{s}\right)-\left\langle h_\mathrm{p}\right\rangle^\mathrm{s}\left\langle\dot{r}'''_{\mathrm{O}_2}\right\rangle \tag{8}$$

The enthalpy of non-stoichiometric ceria is calculated from:

$$h_\mathrm{p}=\left(\bar{h}_{\mathrm{CeO}_2}-\frac{\Delta\delta}{2}\bar{h}_{\mathrm{O}_2}+\Delta\bar{h}_{\mathrm{O}_2}\right)\Big/M_{\mathrm{CeO}_{2-\delta}} \tag{9}$$

where $\Delta\bar{h}_{\mathrm{O}_2}$ is the molar enthalpy of the reduction reaction (Eq. (1)), and $\bar{h}_{\mathrm{O}_2}$ is the molar enthalpy of oxygen. Correlations for $\Delta\bar{h}^\mathrm{o}_{\mathrm{O}_2}$, $\bar{h}_{\mathrm{O}_2}$, and $\bar{h}_{\mathrm{CeO}_2}$ are given in section V.

The interphase heat transfer via the oxygen release is given by:

$$\left\langle\dot{q}'''_{\mathrm{O}_2}\right\rangle=-\left\langle\dot{r}'''_{\mathrm{O}_2}\right\rangle h_{\mathrm{O}_2,\mathrm{sf}} \tag{10}$$

The convective heat transfer between solid and gas phase, $\left\langle\dot{q}'''_\mathrm{conv}\right\rangle$, is described by:

$$\left\langle\dot{q}'''_\mathrm{conv}\right\rangle=f_\mathrm{v}a_\mathrm{p}h_\mathrm{conv}\left(\left\langle T_\mathrm{p}\right\rangle^\mathrm{s}-\left\langle T_\mathrm{g}\right\rangle^\mathrm{g}\right) \tag{11}$$

Inserting eqs. (8), (10) and (11) into eq. (7) yields:

$$f_\mathrm{v}\left\langle\rho_\mathrm{p}\right\rangle^\mathrm{s}c_{p,\mathrm{p}}\frac{\partial}{\partial t}\left(\left\langle T_\mathrm{p}\right\rangle^\mathrm{s}\right)-\left\langle h_\mathrm{p}\right\rangle^\mathrm{s}\left\langle\dot{r}'''_{\mathrm{O}_2}\right\rangle=-\left\langle\dot{r}'''_{\mathrm{O}_2}\right\rangle h_{\mathrm{O}_2,\mathrm{sf}}-f_\mathrm{v}a_\mathrm{p}h_\mathrm{conv}\left(\left\langle T_\mathrm{p}\right\rangle^\mathrm{s}-\left\langle T_\mathrm{g}\right\rangle^\mathrm{g}\right)-\left\langle\nabla\cdot\dot{\mathbf{q}}''_\mathrm{rad}\right\rangle \tag{12}$$

The radiative source term, $-\left\langle\nabla\cdot\dot{\mathbf{q}}''_\mathrm{rad}\right\rangle$, is given in the next section.

The energy balance solved for the gas phase is:

$$(1-f_\mathrm{v})\frac{\partial}{\partial t}\left(\left\langle\rho_\mathrm{g}\right\rangle^\mathrm{g}\left\langle h_\mathrm{g}\right\rangle^\mathrm{g}\right)=-\left\langle\dot{q}'''_{\mathrm{O}_2}\right\rangle+\left\langle\dot{q}'''_\mathrm{conv}\right\rangle \tag{13}$$

Using $\frac{\partial}{\partial t}\left(\left\langle\rho_\mathrm{g}\right\rangle^\mathrm{g}\right)\approx 0$, $\frac{\partial}{\partial t}\left(\left\langle h_\mathrm{g}\right\rangle^\mathrm{g}\right)\approx c_{p,\mathrm{g}}\frac{\partial}{\partial t}\left(\left\langle T_\mathrm{g}\right\rangle^\mathrm{g}\right)$, and eqs. (10) and (11) yields:

$$(1-f_{\mathrm{v}})\left\langle\rho_{\mathrm{g}}\right\rangle^{\mathrm{g}} c_{p,\mathrm{g}}\frac{\partial}{\partial t}\left(\left\langle T_{\mathrm{g}}\right\rangle^{\mathrm{g}}\right)=\left\langle\dot{r}'''_{\mathrm{O_2}}\right\rangle h_{\mathrm{O_2,sf}}+f_{\mathrm{v}}a_{\mathrm{p}}h_{\mathrm{conv}}\left(\left\langle T_{\mathrm{p}}\right\rangle^{\mathrm{s}}-\left\langle T_{\mathrm{g}}\right\rangle^{\mathrm{g}}\right) \tag{14}$$

C. Radiative heat transfer

The radiative transfer equation takes into account radiation emission, absorption, and anisotropic scattering [77]:

$$\frac{\mathrm{d}I_\lambda}{\mathrm{d}s}=\kappa_\lambda I_{\mathrm{b}\lambda}-\kappa_\lambda I_\lambda-\sigma_{\mathrm{s}\lambda}I_\lambda+\frac{\sigma_{\mathrm{s}\lambda}}{4\pi}\int_{4\pi}I_\lambda(\hat{\mathbf{s}}_{\mathrm{i}})\Phi_\lambda(\hat{\mathbf{s}}_{\mathrm{i}},\hat{\mathbf{s}})\mathrm{d}\Omega_i \tag{15}$$

Integration over all solid angles and wavelengths yields the radiative source term:

$$\nabla\cdot\dot{\mathbf{q}}''_{\mathrm{rad}}=\int_0^\infty\kappa_\lambda\left(4\pi I_{\mathrm{b}\lambda}-\int_{4\pi}I_\lambda(\hat{\mathbf{s}})\mathrm{d}\Omega\right)\mathrm{d}\lambda \tag{16}$$

The radiative source term is evaluated numerically as described in section VI.

For the range of values for the size parameter, $x=2\pi r_{\mathrm{p}}/\lambda$, encountered in the present system, $1\le x\le 10^2$, the Mie theory is employed to calculate the scattering and absorption efficiency factors, Q_{s} and Q_{a}, and the scattering phase function, Φ [78],[79]. The efficiency factors are related to the scattering and absorption coefficients via:

$$\sigma_{\mathrm{s}\lambda}=\frac{3}{4}\frac{f_{\mathrm{v}}}{r_{\mathrm{p}}}Q_{\mathrm{s}\lambda} \tag{17a}$$

$$\kappa_\lambda=\frac{3}{4}\frac{f_{\mathrm{v}}}{r_{\mathrm{p}}}Q_{\mathrm{a}\lambda} \tag{17b}$$

D. Convective heat transfer

This study is limited to particle diameters in the range $1-20\,\mu\mathrm{m}$ and particle volume fractions in the range $10^{-4}-10^{-6}$. Hence, the minimum fluidizing $\mathrm{Re_p}$ number is $<10^{-3}$ in all cases, and the fluid flow around an individual particle can be considered independent of the presence of the surrounding particles. For heat transfer between single particles and gas, $\mathrm{Nu_p}\approx 2$, as long as $\mathrm{Re_p}<0.1$ (corresponding to gas velocity $<1\,\mathrm{m\,s^{-1}}$) [80]. Here, it is assumed that $\mathrm{Re_p}<0.1$ and hence $\mathrm{Nu_p}=2$.

E. Boundary and initial conditions

The boundary conditions for the energy equation of the solid phase are:

$$T_{\mathrm{surr}} = 0\ \mathrm{K}, \quad \varepsilon_{\mathrm{surr}} = 1, \quad \dot{q}''_{\mathrm{i}}(z=0) = C\,\dot{q}''_{\mathrm{solar}} \tag{18}$$

The initial temperature of the particles and the gas is set arbitrarily:

$$\left\langle T_{\mathrm{p}}\left(t=0, 0 \le z \le L\right)\right\rangle^{\mathrm{s}} = \left\langle T_{\mathrm{g}}\left(t=0, 0 \le z \le L\right)\right\rangle^{\mathrm{g}} = T_0 \tag{19}$$

Initially, the particles are assumed to be in chemical equilibrium. The equilibrium non-stoichiometry of ceria is a function of temperature and oxygen partial pressure [81]:

$$\Delta\bar{g}^{\mathrm{o}}_{\mathrm{O_2}}(\delta) = \Delta\bar{h}^{\mathrm{o}}_{\mathrm{O_2}}(\delta) - T\Delta\bar{s}^{\mathrm{o}}_{\mathrm{O_2}}(\delta) = \bar{R}T\ln\left(p_{\mathrm{O_2}}/p_{\mathrm{ref}}\right) \tag{20}$$

Equation (20) with $T = T_0$ and $p_{\mathrm{O_2}}$ equal to the initial oxygen partial pressure in the gas phase, $p_{\mathrm{O_2},0}$, yields the initial non-stoichiometry, $\langle\delta_0\rangle^{\mathrm{s}}$, and eq. (5) yields the initial density, $\langle\rho_{\mathrm{p},0}\rangle^{\mathrm{s}}$, of the particles.

IV. Chemical kinetics

A rate expression for the reaction given by Eq. (1) was derived by Keene et al. [76]. In a first step, an expression for the equilibrium constant of the oxygen uptake/release reaction by the ceria was formulated under the assumptions that the oxygen vacancies in the ceria lattice are doubly ionized and that the system behaves like an ideal solution [13]. Further applying crystal site conservation, electroneutrality, and the law of mass action, an expression was derived for the interphase enthalpy flux associated with the oxygen release by the particles, which is a function of the solid temperature, gas-phase oxygen partial pressure, oxygen non-stoichiometry in the solid, and an unknown kinetic rate constant, $\dot{n}''_{\mathrm{sf}}$:

$$\dot{m}''_{\mathrm{sf,O_2}} h_{\mathrm{O_2,sf}} = \frac{M_{\mathrm{O_2}}}{2}\dot{n}''_{\mathrm{sf}}\left(\langle\delta\rangle^{\mathrm{s}}\right)^3\left[\exp\left(\frac{1}{2}\frac{\Delta\bar{h}^{\mathrm{o}}_{\mathrm{O_2}} - \langle T_{\mathrm{p}}\rangle^{\mathrm{s}}\Delta\bar{s}^{\mathrm{o}}_{\mathrm{O_2}}}{\bar{R}\langle T_{\mathrm{p}}\rangle^{\mathrm{s}}}\right)h_{\mathrm{O_2}}\Big|_{\langle T_{\mathrm{p}}\rangle^{\mathrm{s}}} - \left(\frac{\langle p_{\mathrm{O_2}}\rangle^{\mathrm{g}}}{p_{\mathrm{ref}}}\right)^{1/2} h_{\mathrm{O_2}}\Big|_{\langle T_{\mathrm{g}}\rangle^{\mathrm{g}}}\right] \tag{21}$$

The kinetic rate constant is treated as a parameter in the present study. The oxygen release rate per unit volume is given by:

$$\left\langle \dot{r}'''_{\mathrm{O_2}}\right\rangle = \dot{m}''_{\mathrm{sf,O_2}}\, a_{\mathrm{p}}\, f_{\mathrm{v}} \tag{22}$$

V. Properties

A. Optical properties

Application of the Mie theory requires the knowledge of the complex refractive index of ceria $m_\lambda = n_\lambda - \mathrm{i}k_\lambda$. Several studies have been conducted to determine m_λ for ceria at room temperature, both experimentally and analytically ([82]–[86] and literature cited therein). In the present model, data for m_λ for dense ceria from three different sources are used and compared: the experimental data obtained by Patsalas et al. [87] for nanocrystalline ceria and by Marabelli & Wachter [88] for mono-crystalline ceria, and the data obtained by Sun et al. [89] from first principle calculations for cubic ceria. The values for the refractive index, n_λ, and the absorptive index, k_λ, used in this study are shown in Fig. 2. The complex refractive index is assumed to be independent of temperature and non-stoichiometry.

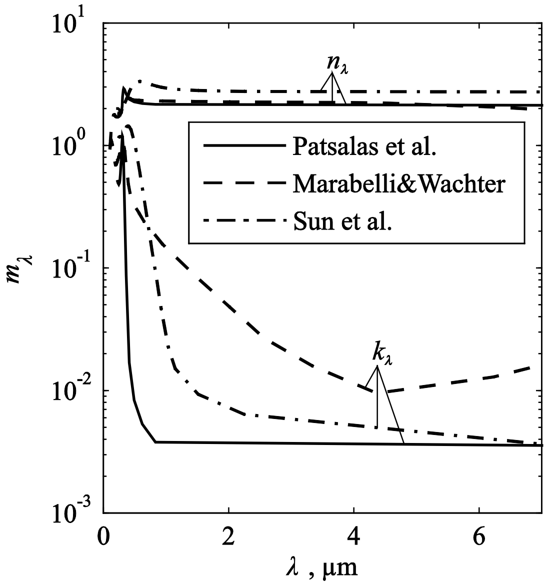

Fig. 2 Complex refractive index of ceria [87–89].

Fig. 3 shows the spectral scattering and absorption coefficients and scattering albedo obtained using the three data sets for the complex refractive index shown in Fig. 2. While the values for the scattering coefficient are comparable for the three models, the absorption coefficient shows significant differences between the models in the visible and infrared wavelength ranges. In addition, Fig. 4 shows the scattering phase function at visible (0.5 μm) and near infrared

(1.3 μm) wavelengths. At all particle diameters and both wavelengths, the particles exhibit a strong backward scattering component (directions <30°) that leads to reflection losses near the entrance plane of the modeling domain, while there is no clear preferred direction over the range of 30 to 180°.

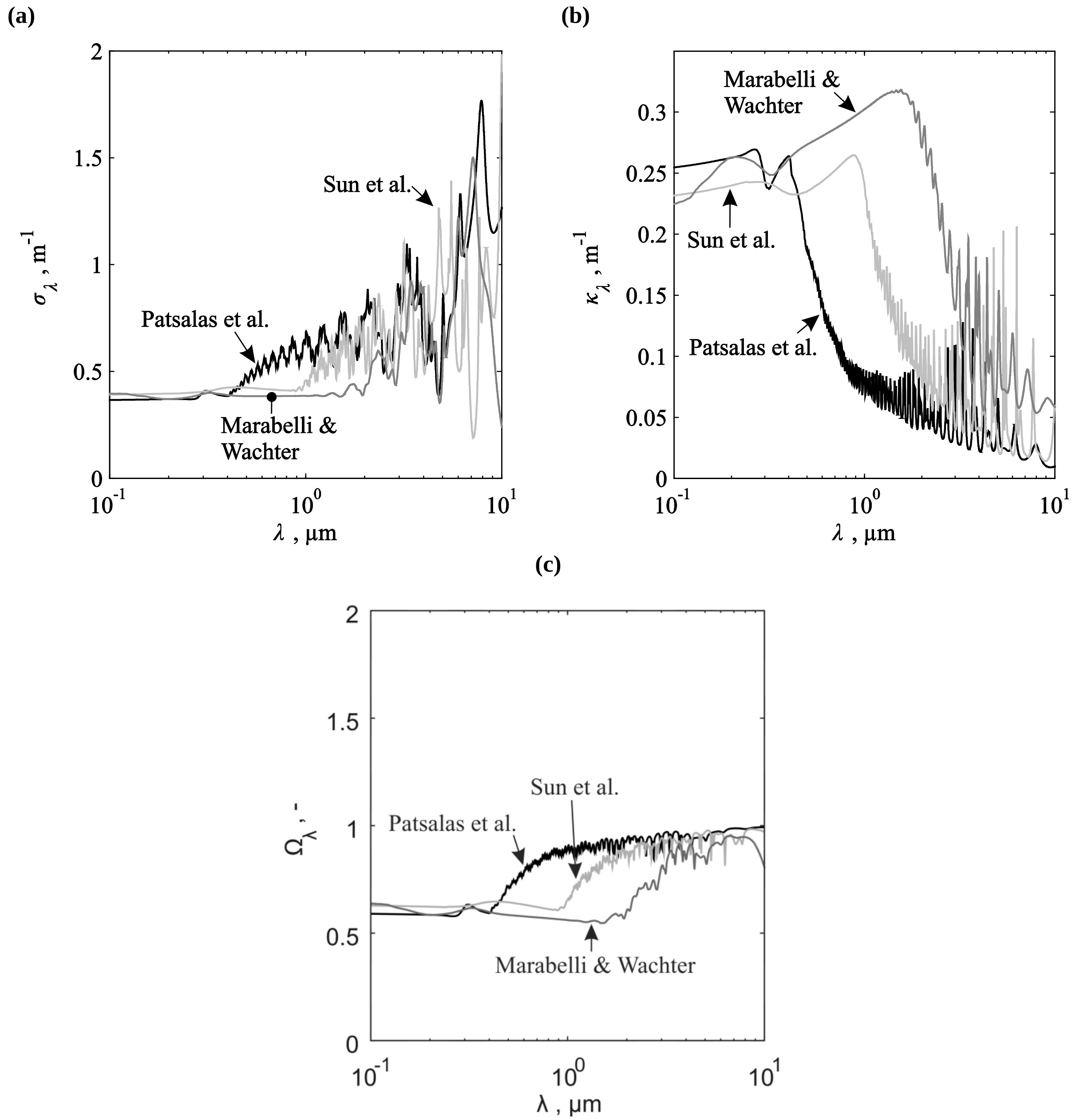

Fig. 3 Spectral scattering (a) and absorption (b) coefficients, and scattering albedo (c) of ceria particles of d_p = 5 μm diameter and $f_v = 10^{-6}$ volume fraction.

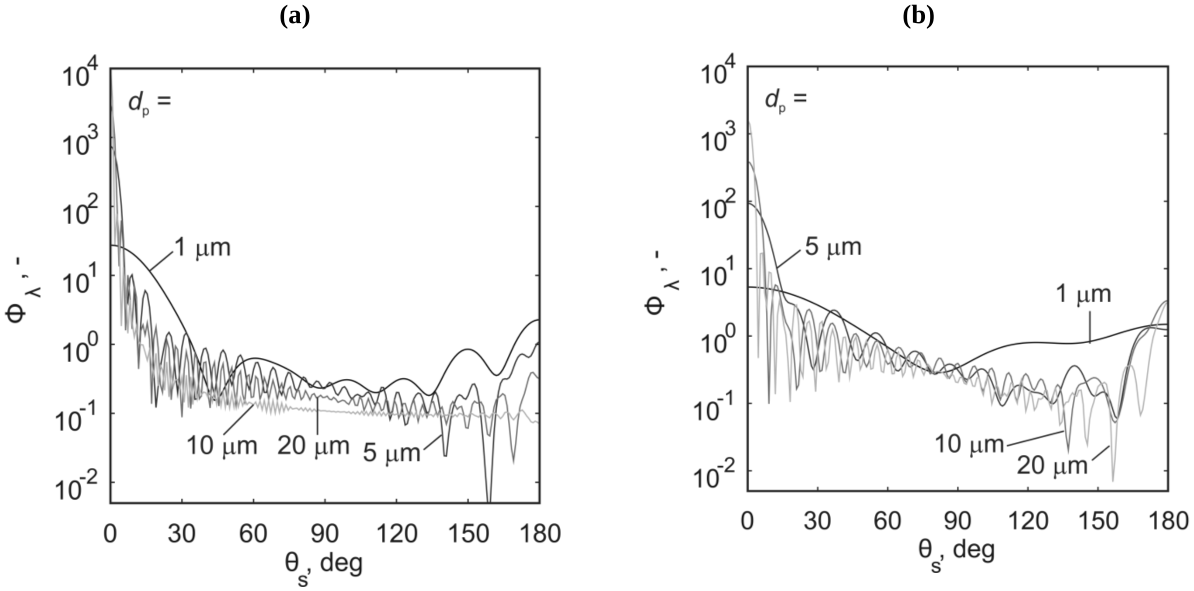

Fig. 4 Scattering phase function for wavelengths of 0.5 μm (a) and 1.3 μm (b) for 4 different particle diameters of d_p = 1, 5, 10 and 20 μm.

B. Thermophysical properties

The enthalpy, $\Delta\bar{h}^{\mathrm{o}}_{\mathrm{O_2}}$, and entropy, $\Delta\bar{s}^{\mathrm{o}}_{\mathrm{O_2}}$, of reaction (1) have been determined experimentally [81]. Correlations to describe the data have been obtained by Keene et al. [76]:

$$\Delta\bar{h}^{\mathrm{o}}_{\mathrm{O_2}}(\delta) = 9.65 \times 10^7 \left(-10.05 + 36.01\delta - 417.15\delta^2 + 4590.21\delta^3 \ldots -31163.99\delta^4 + 99198.37\delta^5 - 115948.36\delta^6\right) \tag{23a}$$

$$\Delta\bar{s}^{\mathrm{o}}_{\mathrm{O_2}}(\delta) = 4184.0\left(11.55\log(\delta) - 70.38 + 224.85\delta - 180.79\delta^2 - 3999.58\delta^3 + 9563.11\delta^4\right) \tag{23b}$$

The specific heat capacity and enthalpy of ceria and oxygen are calculated with the following correlations, with the parameters listed in Table 1 [90]:

$$\bar{c}_p = c_0 + c_1T + c_2T^2 + c_3T^{-2} \tag{24a}$$

$$\bar{h}(T) = \bar{h}_{\mathrm{f}} + c_0\left(T - T_{\mathrm{ref}}\right) + 1/2\,c_1\left(T^2 - T_{\mathrm{ref}}^2\right) + 1/3\,c_2\left(T^3 - T_{\mathrm{ref}}^3\right) - c_3\left(T^{-1} - T_{\mathrm{ref}}^{-1}\right) \tag{24b}$$

Table 1 Parameters in Eqs. (24) to calculate the specific heat capacity and enthalpy of ceria and molecular oxygen [90]

Parameter	Ceria	Oxygen
c_0	64.81×10^3	29.15×10^3
c_1	17.7	6.48
c_2	0	-1.02×10^{-3}
c_3	-0.76×10^9	-0.18×10^9
$\bar{h}_\mathrm{f}$ (J kmol^{-1})	-1088.7×10^6	0
T_ref (K)	298	298

VI. Numerical solution

The computational domain is divided into N_cv ($j = 1...N_\mathrm{cv}$) layers of equal thickness Δz. The governing equations are integrated in space using the finite-volume method and over time using the ODE solution algorithm developed and implemented by Shampine and Gordon [91],[92]. The radiative source term, $-\left\langle \nabla \cdot \dot{\mathbf{q}}''_\mathrm{rad} \right\rangle$, is determined in every time step using the energy-portioning Monte Carlo ray tracing method [93]. This involves the emission of a prescribed number of ray bundles from within the computational domain as well as from its boundaries and following their paths through the participating medium until their power is reduced by absorption below a threshold level or they are lost through the medium boundaries. Alternatively, a differential method could be used [94]. Thermophysical properties are updated in every time step.

A. Integrated mass and energy conservation equations

The discrete, volume-integrated governing equations, Eqs. (3), (12) and (14), are:

$$\frac{\partial \left\langle \rho_{\mathrm{p},j} \right\rangle^\mathrm{s}}{\partial t} = -\frac{1}{f_\mathrm{v}} \left\langle \dot{r}'''_{\mathrm{O}_2,j} \right\rangle \tag{25}$$

$$\frac{\partial}{\partial t}\left(\left\langle T_{\mathrm{p},j}\right\rangle^{\mathrm{s}}\right)=\frac{1}{f_v\left\langle \rho_{\mathrm{p},j}\right\rangle^{\mathrm{s}} c_{p,\mathrm{p},j}}\left[\left\langle \dot{r}'''_{\mathrm{O}_2,j}\right\rangle\left(\left\langle h_{\mathrm{p},j}\right\rangle^{\mathrm{s}}-h_{\mathrm{O}_2,\mathrm{sf},j}\right)-f_{\mathrm{v}}a_{\mathrm{p}}h_{\mathrm{conv}}\left(\left\langle T_{\mathrm{p},j}\right\rangle^{\mathrm{s}}-\left\langle T_{\mathrm{g},j}\right\rangle^{\mathrm{g}}\right)-\frac{1}{A_{\mathrm{cv}}\Delta z}\int_{V_{\mathrm{cv},j}}\left\langle \nabla\cdot\mathbf{q}''_{\mathrm{rad}}\right\rangle \mathrm{d}V\right] \tag{26}$$

$$\frac{\partial}{\partial t}\left(\left\langle T_{\mathrm{g},j}\right\rangle^{\mathrm{g}}\right)=\frac{1}{\left(1-f_{\mathrm{v}}\right)\left\langle \rho_{\mathrm{g},j}\right\rangle^{\mathrm{g}} c_{p,\mathrm{g},j}}\left[\left\langle \dot{r}'''_{\mathrm{O}_2,j}\right\rangle h_{\mathrm{O}_2,\mathrm{sf},j}+f_{\mathrm{v}}a_{\mathrm{p}}h_{\mathrm{conv}}\left(\left\langle T_{\mathrm{p},j}\right\rangle^{\mathrm{s}}-\left\langle T_{\mathrm{g},j}\right\rangle^{\mathrm{g}}\right)\right] \tag{27}$$

B. Radiation emission inside the medium

Prescribing $N_{\mathrm{ray,e}}$, the total number of ray bundles traced in each time step to represent the radiative power emitted within the medium, the radiative power carried by a ray bundle at the point of emission is:

$$\dot{q}_{\mathrm{ray,e}}=\frac{1}{N_{\mathrm{ray,e}}}\int_V 4\kappa_{\mathrm{P}}\sigma T^4\mathrm{d}V \tag{28}$$

The model domain is discretized into N_{cv} ($j=1,\ldots,N_{\mathrm{cv}}$) isothermal layers of unit cross-section and thickness Δz, $V_{\mathrm{cv}}=A_{\mathrm{cv}}\Delta z$, where $A_{\mathrm{cv}}=1\mathrm{m}^2$, with uniform properties in each layer. The discrete form of Eq. (28) is:

$$\dot{q}_{\mathrm{ray,e}}=\frac{1}{N_{\mathrm{ray,e}}}\sum_{j=1}^{N_{\mathrm{cv}}}4\kappa_{\mathrm{P},j}\sigma\left(\left\langle T_{\mathrm{p},j}\right\rangle^{\mathrm{s}}\right)^4 V_{\mathrm{cv}}=\frac{A_{\mathrm{cv}}\Delta z}{N_{\mathrm{ray,e}}}\sum_{j=1}^{N_{\mathrm{cv}}}4\kappa_{\mathrm{P},j}\sigma\left(\left\langle T_{\mathrm{p},j}\right\rangle^{\mathrm{s}}\right)^4 \tag{29}$$

The number of rays emitted from within layer j is found from:

$$N_{\mathrm{ray,e},j}=\mathrm{nint}\left(\frac{1}{\dot{q}_{\mathrm{ray,e}}}\int_{V_{\mathrm{cv},j}}4\kappa_{\mathrm{P}}\sigma T_{\mathrm{p}}^4\mathrm{d}V\right)=\mathrm{nint}\left(\frac{1}{\dot{q}_{\mathrm{ray,e}}}4\kappa_{\mathrm{P},j}\sigma\left(\left\langle T_{\mathrm{p},j}\right\rangle^{\mathrm{s}}\right)^4 A_{\mathrm{cv}}\Delta z\right) \tag{30}$$

with $\dot{q}_{\mathrm{ray,e}}$ obtained from Eq. (29). The location of emission of a ray bundle within layer j is determined from:

$$z_{\mathrm{e},j}=\left(j-1+\Re\right)\Delta z \tag{31}$$

where $\Re$ denotes a random number from the uniform range $\left(0,1\right)$. The direction of emission in polar coordinates is found from:

$$\varphi=2\pi\Re \tag{32a}$$

$$\theta = \cos^{-1}\left(1-2\Re\right) \tag{32b}$$

The wavelength λ of an emitted ray is determined from:

$$\Re = \frac{1}{\kappa_{\mathrm{P},j}\sigma\left(\left\langle T_{\mathrm{p},j}\right\rangle^{\mathrm{s}}\right)^{4}}\int_{0}^{\lambda}\kappa_{\lambda}\left(\lambda^{*},\left\langle T_{\mathrm{p},j}\right\rangle^{\mathrm{s}},p\right)E_{\lambda\mathrm{b}}\left(\lambda^{*},\left\langle T_{\mathrm{p},j}\right\rangle^{\mathrm{s}}\right)\mathrm{d}\lambda^{*} \tag{33}$$

C. Externally incident radiation

Concentrated solar radiation is assumed to be incident at $z = 0$ with direction parallel to the z-axis.[1] Prescribing the solar concentration ratio C and the number $N_{\mathrm{ray,i}}$ of rays traced in each time step to simulate the incident solar radiation, the radiative power carried by a ray bundle at $z=0$ is:

$$\dot{q}_{\mathrm{ray,i}} = \frac{C\,G_{\mathrm{b}}A_{\mathrm{cv}}}{N_{\mathrm{ray,i}}} \tag{34}$$

D. Ray tracing

The ray's travel distance within the medium, s, between two attenuation points is obtained by numerically solving:

$$\Re = \frac{I_{\lambda}\left(s\right)}{I_{\lambda}\left(0\right)} = \exp\left(-\int_{0}^{s}\beta_{\lambda}\left(s^{*}\right)\mathrm{d}s^{*}\right) \tag{35}$$

At the location of attenuation, the energy carried by the ray, q_{ray}, is partitioned into absorbed and scattered fractions according to:

$$\dot{q}_{\mathrm{ray,a}} = \left(1-\omega_{\lambda}\right)q_{\mathrm{ray}} \tag{36a}$$

$$\dot{q}_{\mathrm{ray,s}} = \omega_{\lambda}\dot{q}_{\mathrm{ray}} \tag{36b}$$

where ω_{λ} is the scattering albedo. The new travel direction of the scattered fraction of the ray is determined relative to the ray travel direction before the attenuation event, using the scattering phase function and random numbers:

---

[1] With an ideal solar concentrator with a concentration ratio of $C = 1000$, the concentrated solar radiation would be incident within a cone half-angle of 8.5°.

$$\Re = \frac{1}{2}\int_{0}^{\theta} \Phi_{\lambda}\left(\theta^{*}\right)\sin\theta^{*}\mathrm{d}\theta^{*} \tag{37a}$$

$$\varphi = 2\pi\Re \tag{37b}$$

The ray tracing of a ray bundle is terminated when the scattered fraction of the ray energy is below 0.01% of the ray's initial energy. Once all $N_{\mathrm{ray,e}} + N_{\mathrm{ray,i}}$ rays have been traced through the model domain, the integrated radiative source term is calculated from:

$$-\int_{V_{\mathrm{cv},j}} \left\langle \nabla \cdot \dot{\mathbf{q}}''_{\mathrm{rad}} \right\rangle \mathrm{d}V = \sum_{i=1}^{N_{\mathrm{a},j}} \dot{q}_{\mathrm{ray,a},j,i} - 4\kappa_{\mathrm{P},j}\sigma\left(\left\langle T_{\mathrm{p},j}\right\rangle^{\mathrm{s}}\right)^{4} A_{\mathrm{cv}}\Delta z \tag{38}$$

The first term corresponds to the radiative energy absorbed in layer j, where $N_{\mathrm{a},j}$ is the total number of attenuation events in layer j (of both, internally emitted and externally incident rays), and $q_{\mathrm{ray,a},j,i}$ is the absorbed energy at each attenuation event. The second term corresponds to the radiative energy emitted from within the layer.

VII. Results

A parametric study has been conducted to analyze the influence of different model parameters on the transient and steady-state temperature and non-stoichiometry distributions in the particle suspension. Table 2 gives an overview of the selected baseline values for the model parameters, and the ranges over which selected parameters were varied. In this study, we varied the following parameters: particle volume fraction, particle diameter, kinetic rate constant, number of control volume layers and source of complex refractive index. The ranges of parameter variation are summarized in Table 2. These parameters are varied one by one, with all other parameters held at their baseline value tabulated in Table 2, unless stated otherwise in the text below.

Volume fraction and particle diameter are basic parameters of the particle suspension. These parameters are expected to have a strong influence on the radiative heat transfer in the particle suspension and can be selected to some degree freely in the design of a solar reactor system. Therefore, it is of interest to analyze their influence and obtain initial order-of-magnitude estimations of their values.

Since the kinetic rate constant is currently unknown, we further study the influence of different possible values on the results, including extreme cases with very low and very high rate. As discussed in the Problem Statement and further below, the current model assumes that particles are layered. This model constraint results in larger non-uniformities across the particle bed than in a well-mixed reactor. To compare the case of stratified particles with the case of an ideally mixed system, we varied the number of control volumes in the *z*-direction from 50 to 1. Finally, since significant differences exist for the optical properties for ceria across different sources, we vary the optical properties to study its significance on the model results.

The time integration step was set to 1×10^{-3} s. The total number of rays traced in each time step, $N_{\mathrm{ray}} = N_{\mathrm{ray,e}} + N_{\mathrm{ray,i}}$, was selected to be 10^{5} or 10^{6}, depending on the optical density of the suspension, in order to achieve low fluctuations in the results. In all cases, the gas temperature closely followed the particle temperature. Therefore, only particle temperatures are presented below.

Table 2 Model parameters

Parameter	Baseline value	Range	
Layer thickness, L (m)	0.1		
Solar concentration ratio, C	1000		
Direct normal irradiance, G_b (W m^{-2})	1000		
Initial temperature, T_0 (K)	300		
Initial oxygen partial pressure, $p_{\mathrm{O_2},0}$ (atm)	10^{-5}		
Total pressure, p (atm)	1		
Volume fraction, f_v	10^{-6}	10^{-6}	10^{-4}
Particle diameter, d_p $(\mu\mathrm{m})$	5	1	20
Kinetic rate constant, $n''_{\mathrm{O_2}}$ $\left(\mathrm{mol\,m^{-2}\,s^{-1}}\right)$	1	0.1	∞
Number of layers, N_cv	50	1	50
Source of complex refractive index, m_λ	Patsalas et al. [87]	Marabelli & Wachter [88]	Sun et al. [89]

The influence of the kinetic rate constant, $\dot{n}''_{O_2}$, on the evolution of the non-stoichiometry is shown in Fig. 5, and compared to the evolution of the temperature profile. All other parameters are set to their baseline value tabulated in Table 2. The temperature evolution is nearly unaffected by the variation in $\dot{n}''_{sf}$. Therefore, only one temperature profile is plotted for all cases. The curve labeled "eq." denotes the limiting case of $\dot{n}''_{O_2} \to \infty$. In this case, the reaction rate is heat transfer-limited, and the non-stoichiometry corresponds to the equilibrium non-stoichiometry, given by Eq. (20), at any time *t*. Below $\dot{n}''_{O_2} = 1$ kmol m^{-2} s^{-1}, the rate constant significantly influences the evolution of the non-stoichiometry, particularly at lower temperatures. For $\dot{n}''_{O_2} = 1$ kmol m^{-2} s^{-1}, the non-stoichiometry profile reaches steady state after approx. 10 s, nearly at the same time as the temperature profile, while with $\dot{n}''_{O_2} = 0.1$ kmol m^{-2}s^{-1} the non-stoichiometry profile takes almost twice as long to reach steady state (after approx. 18 s; not shown on graph).

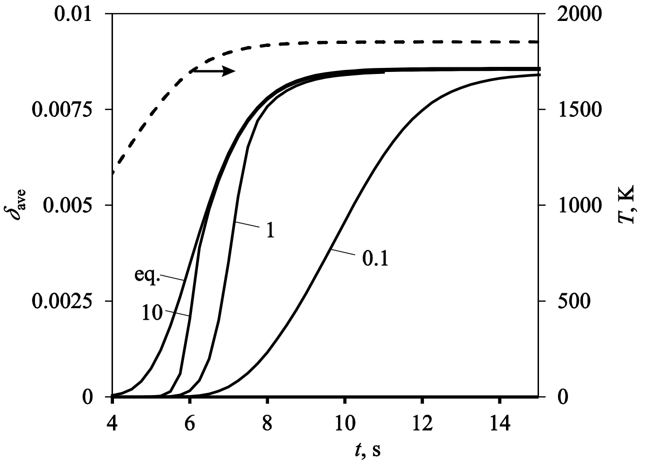

Fig. 5 Evolution of average non-stoichiometry (solid curves/left *y*-axis) and temperature (dashed curve/right *y*-axis) for different kinetic rate constants.

The evolution of the temperature profile in the particle suspension is shown in Fig. 6 for different particle volume fractions: (a) f_v=10^{-6}, (b) f_v=10^{-5}, and (c) f_v=10^{-4}, with all other parameters at their baseline value tabulated in Table 2. The gray curves show the transient temperature profiles at different time intervals $\Delta\tau$: (a): $\Delta\tau$ =1 s, (b)–(c): $\Delta\tau$ =0.25 s. The black curves are the steady-state temperature profiles. The red curves are the temperature profiles after 1 s. The time to reach the steady-state temperature distribution is indicated above the black curve, which is the asymptotic temperature profile reached at steady state. At a low particle volume fraction of $f_\mathrm{v} = 10^{-6}$, the particle suspension has low thermal capacity but also low optical thickness and hence retains a low fraction of the incident solar radiation. This results in a low heating rate and uniform temperature distribution. At particle volume fractions of $f_\mathrm{v} = 10^{-5}$ and 10^{-4}, the thermal capacity of the particle suspension is still relatively low, while the optical thickness strongly increases, resulting in increased heating rate and increasing temperature non-uniformities. This is further illustrated by the steady-state energy balances for the two cases with $f_\mathrm{v} = 10^{-6}$ and $f_\mathrm{v} = 10^{-4}$ listed in Table 3. With $f_\mathrm{v} = 10^{-6}$, the suspension absorbs only 1.4% of the incident solar radiation, while the remainder is transmitted or reflected (the scattering and absorption coefficients are proportional to the volume fraction, Eqs. (17)). In contrast, for $f_\mathrm{v} = 10^{-4}$, 75% of the incident solar radiation is absorbed and re-radiated to the environment by the particle suspension, leading to a higher peak temperature at equilibrium (Fig. 6). For the case of $f_\mathrm{v} = 10^{-4}$, which leads to significant temperature non-uniformity (Figs. 6c), the peak equilibrium temperature occurs at a short distance from the irradiated boundary ($z/L = 0$), where the incident solar radiative flux is high and the particles are surrounded by other hot particles.

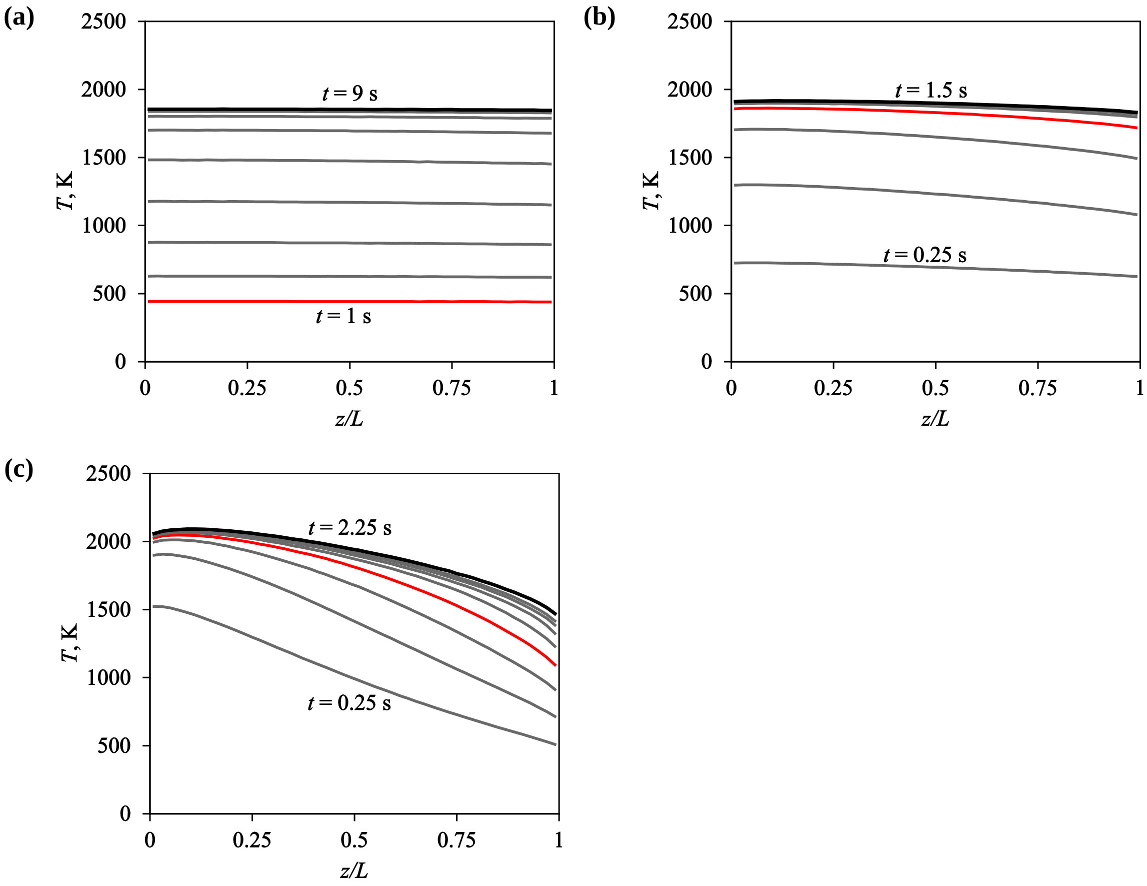

Fig. 6 Evolution of the temperature profile in the particle suspension for different particle volume fractions:

(a) $f_v=10^{-6}$, (b) $f_v=10^{-5}$, and (c) $f_v=10^{-4}$.

Table 3 Comparison of the steady–state energy balances (in % of the incident solar power) for the cases with volume fractions of f_v=10^{-6} and f_v =10^{-4}

Volume fraction f_v	Radiation transmitted, %	Radiation absorbed and re-radiated (left / right), %	Radiation reflected, %
10^{-6}	98	1.4 (0.7 / 0.7)	0.6
10^{-4}	9.8	75.1 (46.8 / 28.3)	15.1

The evolution of the non-stoichiometry distribution in the particle suspension is shown Figs. 7a–c for three selected particle volume fractions: (a) f_v=10^{-6}, (b) f_v=10^{-5}, and (c) f_v=10^{-4}, with all other parameters at their baseline value tabulated in Table 2. The initial non-stoichiometry is $\langle \delta_0 \rangle \approx 0$. The gray curves show the transient non-stoichiometry distributions at different time intervals $\Delta\tau$: (a): $\Delta\tau$ = 0.5 s, (b)–(c): $\Delta\tau$ = 0.25 s. The black curves are the final non-stoichiometry distributions. The red curves are the non-stoichiometry distributions after 1 s. With particle volume fractions of $f_v = 10^{-5}$ and 10^{-4} and fast heating rates, the non-stoichiometry distribution takes slightly longer to reach steady state than the temperature distribution, suggesting that the process is limited by chemical kinetics rather than by the heating rate, for the selected parameters. In contrast, with particle volume fraction of $f_v = 10^{-6}$ and lower heating rate, the non-stoichiometry distribution takes approximately the same time to reach steady state as the temperature profile, indicating that the process is heat transfer limited. From Eq. (20), it results that the equilibrium non-stoichiometry strongly depends on the particle temperature. This leads to strong non-uniformities in the non-stoichiometry distribution within the particle suspension even for relatively uniform temperature distributions such as for $f_v = 10^{-5}$ and 10^{-4}. In regions where the temperature remains below approx. 1700 K, particles do not react to a significant extent (Figs. 6c / 7c).

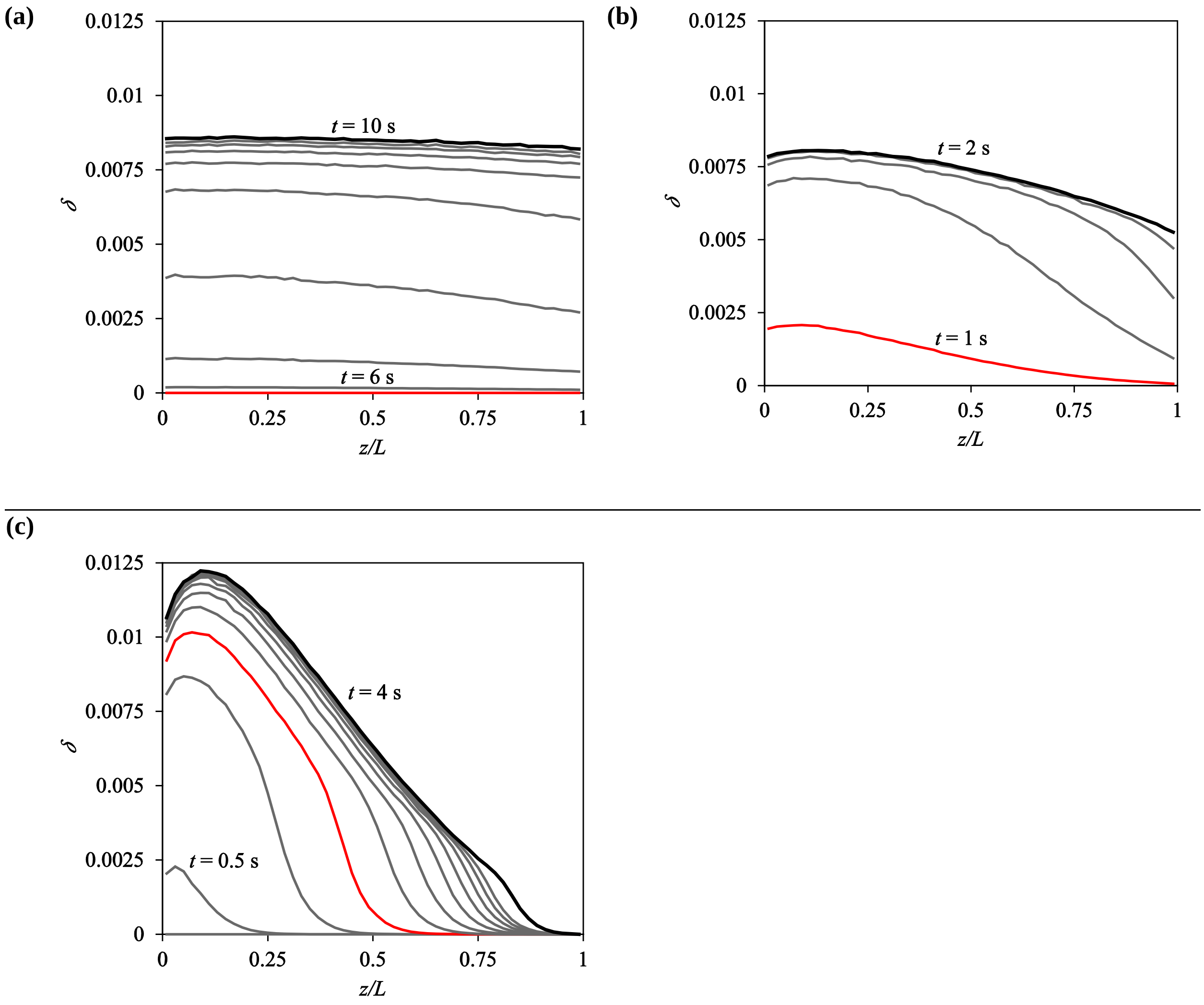

Fig. 7 Evolution of the non-stoichiometry distribution in the particle suspension for four three selected particle volume fractions: (a) f_v=10^{-6}, (b) f_v=10^{-5}, and (c) f_v=10^{-4}**.**

The reaction rate, Eq. (22), also strongly depends on the particle temperature. This is illustrated by the temperature and non-stoichiometry profiles after 1 s for the two cases with $f_{\mathrm{v}} = 10^{-5}$ and 10^{-4}, indicated in red in Figs. 6b–c and 7b–c. While at this instant the peak temperature in case b) is 1863 K and less than 10% below that in case c), the non-stoichiometry is more than 70% lower. The effect of the temperature dependence of the reaction rate can also be observed from the transient curves in Fig. 7c after 2.25 s of simulation time, i.e. after the temperature profile has reached steady state. Near $z/L = 0$, where the temperature is highest, the steady-state non-stoichiometry has nearly been reached after 2.25 s of simulation time, whereas the non-stoichiometry is still far away from the steady-state profile in the cooler regions near $z/L = 1$.

These results illustrate two important aspects for the design of a particle-based solar reactor. One, for low particle volume fractions in the order of $f_{\mathrm{v}} = 10^{-6}$ and hence low optical thickness of the particle bed, the particle bed should be contained in an effective light trap, i.e. a cavity-type solar receiver-reactor, which allows for multiple internal reflections and hence multiple ray passes through the particle bed. Two, the strong non-uniformities of temperature and non-stoichiometry across the particle bed at higher particle bed densities (volume fraction of $f_{\mathrm{v}} = 10^{-4}$ or higher) that result with our current model emphasize the importance for effective particle/gas mixing.

However, despite the large differences in the non-stoichiometry distributions, the average equilibrium non-stoichiometry in the particle suspension varies by only 25% among the three cases shown in Fig. 7.

Fig. 8 shows the evolution of the temperature profile in the particle suspension for four selected particle diameters: (a) d_{p}=1 μm, (b) d_{p}=5 μm, (c) d_{p}=10 μm, and (d) d_{p}=20 μm, with all other parameters at their baseline value tabulated in Table 2. The gray curves show the transient temperature profiles at different time intervals $\Delta\tau$: (a)–(c): $\Delta\tau$ = 1 s, (d): $\Delta\tau$ = 2 s. The black curves are the steady-state temperature profiles. Decreasing particle diameter leads to increasing absorption and scattering coefficients, particularly over the spectrum relevant for solar radiation. This leads to increasing heating rate, higher steady-state temperature, and faster reaction rate with decreasing particle diameter. The latter can be seen in Fig. 9, which shows the evolution of the average non-stoichiometry in the particle suspension for different particle diameters, with all other parameters at their baseline value tabulated in Table 2. Despite the increasing radiation attenuation with decreasing particle diameter, the temperature distribution remains relatively uniform in all cases considered. These results indicate that, within certain limits, the heating and reaction rates can be accelerated by decreasing the particle diameter without significantly affecting the temperature and hence the non-stoichiometry uniformity in the particle bed and hence without the requirement for strong particle/gas mixing.

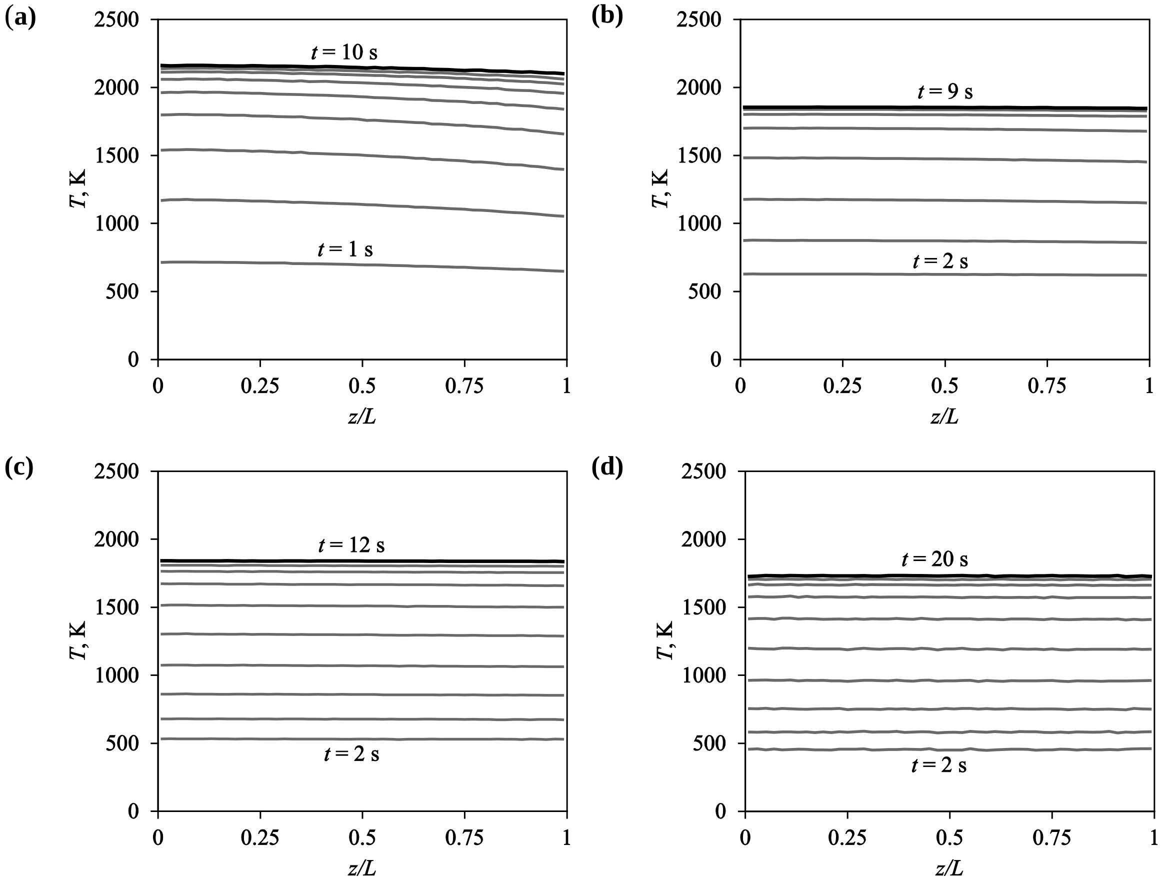

Fig. 8 Evolution of the temperature profile in the particle suspension for four selected particle diameters: (a) d_p=1 μm, (b) d_p=5 μm, (c) d_p=10 μm, and (d) d_p=20 μm**.**

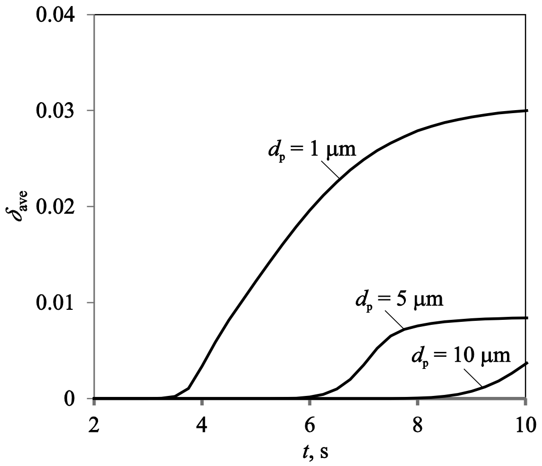

Fig. 9 Evolution of the average non-stoichiometry in the particle suspension for different particle diameters.

The baseline case assumes that every particle is confined to one of the N_{cv} parallel layers across the bed thickness (*z*-direction in Fig. 1). Such a situation can be representative of suspended or falling particles whose trajectories are relatively undisturbed by the gas flow. On the other hand, if the particles are intensely mixed by the gas flow, the particle suspension can be assumed to be perfectly mixed. This case is represented with $N_{\mathrm{cv}} = 1$, i.e. the modeling domain is not spatially resolved in *z*-direction and consists only of one single infinite slab. In this configuration, all intensive properties, such as temperature, oxygen non-stoichiometry, oxygen partial pressure, etc. are uniform across the particle bed. Fig. 10 compares the transient temperature distributions in the particle suspension for the cases with (a) $N_{\mathrm{cv}} = 1$ (ideal mixing) and (b) $N_{\mathrm{cv}} = 50$ (particles stratified), with all other parameters at their baseline value tabulated in Table 2, except for the volume fraction, $f_\mathrm{v} = 10^{-4}$. The gray curves show the transient temperature profiles at the time interval $\Delta\tau$ = 0.25 s. The black curves are the steady-state temperature profiles. Fig. 10 shows that with ideal mixing $\left(N_{\mathrm{cv}} = 1\right)$, the steady-state temperature is significantly lower than when the particles are assumed to be stratified, as the absorbed radiation is distributed uniformly across the bed, while steady state is reached within nearly the same time in both cases.

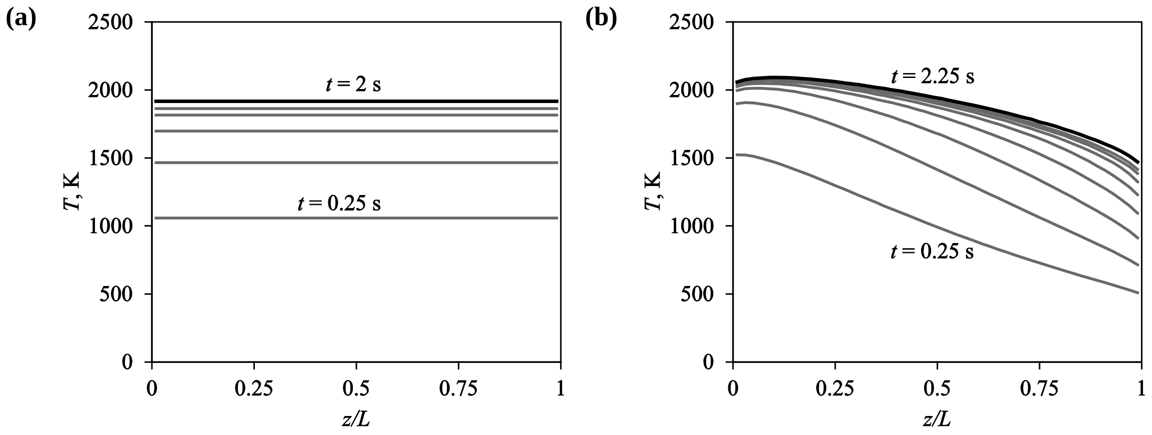

Fig. 10 Evolution of the temperature profile in the particle suspension for different mixing assumptions: (a) mixed particles and (b) stratified particles.

The transient temperature distributions in the particle suspension obtained with the three different data sets are shown in Fig. 11: (a) Patsalas et al. [87], (b) Sun et al. [89], and (c) Marabelli & Wachter [88], with all other parameters at their baseline value tabulated in Table 2. The gray curves show the transient temperature profiles at the time interval $\Delta\tau$ = 1 s. The black curves are the steady-state temperature profiles. Higher absorption coefficient in the visible (0.4–0.7 μm) and near-infrared (0.7–1.4 μm) wavelength ranges leads to stronger absorption of solar radiation by the particle suspension, which results in higher heating rates. On the other hand, higher absorption coefficient in the near- and mid-infrared regions also leads to higher radiation emission by the particle suspension, which results in lower equilibrium temperature.

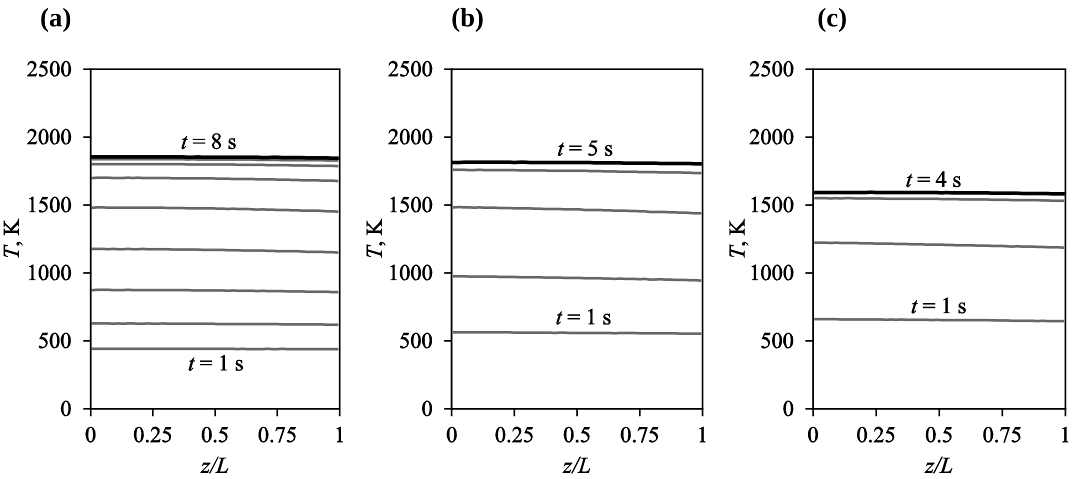

Fig. 11 Evolution of the temperature profile in the particle suspension for different underlying data sets for the complex refractive index, m_λ , taken from: (a) Patsalas et al. [87], (b) Sun et al. [89], and (c) Marabelli & Wachter [88].

VIII. Summary and conclusions

Unsteady partial thermal reduction of a suspension of ceria particles under concentrated solar radiation has been investigated numerically. The particle suspension has been modeled as a 1-D infinite slab, externally irradiated at one boundary, with non-participating surroundings. The slab has been resolved spatially across its thickness with $N_{\mathrm{cv}} = 50$ control volumes. This corresponds to the situation wherein particles are stratified and remain unmixed, thus constituting a worst case in terms of the mixing of the particle bed properties such as temperature and non-stoichoimetry. For comparison, a case with well-mixed conditions is also simulated by setting the number of control volumes across the bed to $N_{\mathrm{cv}} = 1$. The evolution of the temperature and non-stoichiometry distributions in the particle suspension has been studied, varying the particle volume fraction and particle diameter, as well as the unknown kinetic rate constant and the mixing regime of the particles, and using three different data sets for the complex refractive index of ceria.

Increasing the particle volume fraction from 10^{-6} to 10^{-4} increases the heat capacity of the particle suspension and its optical thickness. Increasing optical thickness increases the radiation absorption rate by the particle suspension. This leads to increasing non-uniformity in the temperature and non-stoichiometry distributions and increasing peak temperature at steady state. Due to the trade-off between increasing heat capacity and increasing radiation absorption rate with increasing particle volume fraction, the heating rate remains nearly unchanged as the particle volume fraction is increased from 10^{-5} to 10^{-4}.

Decreasing particle diameter leads to increasing optical thickness of the particle suspension, resulting in increasing average steady-state particle temperature, without strongly affecting the temperature uniformity. A decrease in the particle diameter from 20 to 1 μm leads to an increase in the average steady-state temperature from 1731 to 2142 K, resulting in an increase in the average non-stoichiometry from 0.0043 to 0.031.

For the baseline model parameters considered in this study and the currently unknown kinetic rate constant $\dot{n}''_{O_2}$ below $1\ \mathrm{kmol\ m^{-2}\ s^{-1}}$, steady-state temperatures are reached faster than steady-state non-stoichiometries, indicating that the reaction rate is limited by chemical kinetics, not by heat transfer.

Three different data sets for the complex refractive index of ceria, which were obtained with different material samples and methods, are used and compared in this study. The different data sets lead to differences in the calculated scattering and absorption coefficients of the particle suspension, which in turn can significantly influence the temperature of the particle suspension.

The results obtained suggest that, when designing a solar reactor to conduct the thermal reduction of ceria, uniform temperature distribution in the particle suspension should be targeted, in order to maximize the material utilization, reach uniform reaction extents, and minimize the risk of overheating particles near the irradiated surface of the reactor. Uniform temperature distribution in the particle suspension is achieved when the particles are well mixed in the system, e.g. through a well-designed gas flow pattern. Good mixing of particles and gas is particularly important under conditions where strong non-uniformities in the temperature and non-stoichiometry profiles across the particle bed are observed under the current modeling assumptions.

Acknowledgments

We thank Dr. Daniel Keene for discussions of the kinetics of non-stoichiometric reduction of ceria. Financial support from the Australian Research Council (ARC Future Fellowship FT140101213 by W. Lipiński) is gratefully acknowledged.

References

[1] Romero, M., and Steinfeld, A., “Concentrating solar thermal power and thermochemical fuels,” Energy & Environmental Science, Vol. 5, No. 11, Oct. 2012, pp. 9234–9245. doi: 10.1039/c2ee21275g.

[2] Fletcher, E. A., “Solarthermal processing: a review,” Journal of Solar Energy Engineering, Vol. 123, No. 2, 2000, pp. 63–74. doi: 10.1115/1.1349552.

[3] Bader, R., and Lipiński, W., “Solar Thermochemical Processes,” *Solar Energy*, G.M. Crawley, ed., New Jersey: World Scientific Publishing, 2016, pp. 345–394. .

[4] Bader, R., and Lipiński, W., *Solar thermal processing*, 2016.

[5] Abanades, S., and Flamant, G., “Thermochemical hydrogen production from a two-step solar-driven water-splitting cycle based on cerium oxides,” Solar Energy, Vol. 80, No. 12, Dec. 2006, pp. 1611–1623. doi: 10.1016/j.solener.2005.12.005.

[6] Chueh, W. C., and Haile, S. M., “Ceria as a thermochemical reaction medium for selectively generating syngas or methane from H2O and CO2,” ChemSusChem, Vol. 2, No. 8, Jan. 2009, pp. 735–739. doi: 10.1002/cssc.200900138.

[7] Le Gal, A., Bion, N., Mercier, T. Le, and Harle, V., “Reactivity of Doped Ceria-Based Mixed Oxides for Solar Thermochemical Hydrogen Generation via Two-Step Water-Splitting Cycles,” Energy & Fuels, Vol. 27, No. 10, 2013, pp. 6068–6078. .

[8] Scheffe, J., Jacot, R., and Patzke, G., “Synthesis, Characterization and Thermochemical Redox Performance of Hf, Zr and Sc Doped Ceria for Splitting CO2,” Journal of Physical Chemistry C, Vol. 117, No. 46, 2013, pp. 24104–24114. doi: 10.1021/jp4050572.

[9] Hao, Y., Yang, C.-K., and Haile, S. M., “Ceria−Zirconia Solid Solutions (Ce1−xZrxO2−δ, x ≤ 0.2) for Solar Thermochemical Water Splitting: A Thermodynamic Study,” Chemistry of Materials, Vol. 26, 2014, pp. 6073–6082. doi: 10.1016/j.matchemphys.2012.11.039.

[10] McDaniel, A. H., Miller, E. C., Arifin, D., Ambrosini, A., Coker, E. N., O’Hayre, R., Chueh, W. C., and Tong, J., “Sr- and Mn-doped LaAlO3−δ for solar thermochemical H2 and CO production,” Energy & Environmental Science, Vol. 6, No. 8, 2013, p. 2424. doi: 10.1039/c3ee41372a.

[11] Scheffe, J. R., Weibel, D., and Steinfeld, A., “Lanthanum − Strontium − Manganese Perovskites as Redox Materials for Solar Thermochemical Splitting of H2O and CO2,” Energy & Fuels, Vol. 27, No. 8, 2013, pp. 4250–4257. doi: 10.1021/ef301923h.

[12] Demont, A., Abanades, S., and Beche, E., “Investigation of perovskite structures as oxygen-exchange redox materials for hydrogen production from thermochemical two-step water-splitting cycles,” Journal of Physical Chemistry C, Vol. 118, No. 24, 2014, pp. 12682–12692. doi: 10.1021/jp5034849.

[13] Chueh, W. C., and Haile, S. M., “A thermochemical study of ceria: exploiting an old material for new modes of energy conversion and CO2 mitigation,” Philosophical Transactions of the Royal Society A: Mathematical, Physical, and Engineering Sciences, Vol. 368, No. 1923, Jul. 2010, pp. 3269–3294. doi: 10.1098/rsta.2010.0114.

[14] Müller, R., and Steinfeld, A., “H2O-splitting thermochemical cycle based on ZnO/Zn-redox: Quenching the effluents from the ZnO dissociation,” Chemical Engineering Science, Vol. 63, No. 1, Jan. 2008, pp. 217–227. doi: 10.1016/j.ces.2007.09.034.

[15] Agrafiotis, C., Roeb, M., Konstandopoulos, A. G., Nalbandian, L., Zaspalis, V. T., Sattler, C., Stobbe, P., and Steele, A. M., “Solar water splitting for hydrogen production with monolithic reactors,” Solar Energy, Vol. 79, No. 4, Oct. 2005, pp. 409–421. doi: 10.1016/j.solener.2005.02.026.

[16] Roeb, M., Säck, J.-P., Rietbrock, P., Prahl, C., Schreiber, H., Neises, M., de Oliveira, L., Graf, D., Ebert, M., Reinalter, W., Meyer-Grünefeldt, M., Sattler, C., Lopez, A., Vidal, A., Elsberg, A., Stobbe, P., Jones, D., Steele, A., Lorentzou, S., Pagkoura, C., Zygogianni, A., Agrafiotis, C., and Konstandopoulos, A. G., “Test operation of a 100 kW pilot plant for solar hydrogen production from water on a solar tower,” Solar Energy, Vol. 85, No. 4, Apr. 2011, pp. 634–644. doi: 10.1016/j.solener.2010.04.014.

[17] Chueh, W. C., Falter, C., Abbott, M., Scipio, D., Furler, P., Haile, S. M., and Steinfeld, A., “High-flux solar-driven thermochemical dissociation of CO2 and H2O using nonstoichiometric ceria,” Science (New York, N.Y.), Vol. 330, No. 6012, Dec. 2010, pp. 1797–1801. doi: 10.1126/science.1197834.

[18] Furler, P., Scheffe, J. R., and Steinfeld, A., “Syngas production by simultaneous splitting of H2O and CO2 via ceria redox reactions in a high-temperature solar reactor,” Energy & Environmental Science, Vol. 5, No. 3, 2012, pp. 6098–6103. doi: 10.1039/c1ee02620h.

[19] Furler, P., Scheffe, J., Gorbar, M., Moes, L., Vogt, U., and Steinfeld, A., "Solar thermochemical CO2 splitting utilizing a reticulated porous ceria redox system," Energy & Fuels, Vol. 26, No. 11, 2012, pp. 7051–7059. doi: 10.1021/ef3013757.

[20] Kaneko, H., Miura, T., Fuse, A., Ishihara, H., Taku, S., Fukuzumi, H., Naganuma, Y., and Tamaura, Y., "Rotary-type solar reactor for solar hydrogen production with two-step water splitting process," Energy & Fuels, Vol. 21, No. 4, 2007, pp. 2287–2293. doi: 10.1021/ef060581z.

[21] Diver, R. B., Miller, J. E., Siegel, N. P., and Moss, T. A., "Testing of a CR5 solar thermochemical heat engine prototype," *ASME 2010 4th International Conference on Energy Sustainability*, Phoenix, AZ: 2010, pp. 97–104. doi: 10.1115/ES2010-90093.

[22] Lapp, J., Davidson, J. H., and Lipiński, W., "Efficiency of two-step solar thermochemical non-stoichiometric redox cycles with heat recovery," Energy, Vol. 37, No. 1, Jan. 2012, pp. 591–600. doi: 10.1016/j.energy.2011.10.045.

[23] Diver, R. B., Miller, J. E., Allendorf, M. D., Siegel, N. P., and Hogan, R. E., "Solar thermochemical water-splitting ferrite-cycle heat engines," Journal of Solar Energy Engineering, Vol. 130, No. 4, 2008, p. 041001–1/8. doi: 10.1115/1.2969781.

[24] Lapp, J., and Lipiński, W., "Transient three-dimensional heat transfer model of a solar thermochemical reactor for H_2O and CO_2 splitting via non-stoichiometric ceria redox cycling," Journal of Solar Energy Engineering, Vol. 136, No. 3, 2014, p. 031006–1/11. doi: 10.1115/1.4026465.

[25] Haueter, P., Moeller, S., Palumbo, R., and Steinfeld, A., "The production of zinc by thermal dissociation of zinc oxide - solar chemical reactor design," Solar Energy, Vol. 67, No. 1–3, 1999, pp. 161–167. doi: 10.1016/S0038-092X(00)00037-2.

[26] Müller, R., Lipiński, W., and Steinfeld, A., "Transient heat transfer in a directly-irradiated solar chemical reactor for the thermal dissociation of ZnO," Applied Thermal Engineering, Vol. 28, No. 5–6, Apr. 2008, pp. 524–531. doi: 10.1016/j.applthermaleng.2007.05.002.

[27] Schunk, L. O., Haeberling, P., Wepf, S., Wuillemin, D., Meier, A., and Steinfeld, A., "A Receiver-Reactor for the Solar Thermal Dissociation of Zinc Oxide," Journal of Solar Energy Engineering, Vol. 130, No. 2, 2008,

p. 021009–1/6. doi: 10.1115/1.2840576.

[28] Schunk, L. O., Lipiński, W., and Steinfeld, A., “Heat transfer model of a solar receiver-reactor for the thermal dissociation of ZnO—Experimental validation at 10kW and scale-up to 1MW,” Chemical Engineering Journal, Vol. 150, No. 2–3, Aug. 2009, pp. 502–508. doi: 10.1016/j.cej.2009.03.012.

[29] Villasmil, W., Meier, A., and Steinfeld, A., “Dynamic Modeling of a Solar Reactor for Zinc Oxide Thermal Dissociation and Experimental Validation Using IR Thermography,” Journal of Solar Energy Engineering, Vol. 136, No. 1, Oct. 2014, p. 010901–1/11. doi: 10.1115/1.4025511.

[30] Gokon, N., Takahashi, S., Yamamoto, H., and Kodama, T., “Thermochemical two-step water-splitting reactor with internally circulating fluidized bed for thermal reduction of ferrite particles,” International Journal of Hydrogen Energy, Vol. 33, No. 9, May 2008, pp. 2189–2199. doi: 10.1016/j.ijhydene.2008.02.044.

[31] Perkins, C., Lichty, P. R., and Weimer, A. W., “Thermal ZnO dissociation in a rapid aerosol reactor as part of a solar hydrogen production cycle,” International Journal of Hydrogen Energy, Vol. 33, No. 2, Jan. 2008, pp. 499–510. doi: 10.1016/j.ijhydene.2007.10.021.

[32] Koepf, E., Advani, S. G., Steinfeld, A., and Prasad, A. K., “A novel beam-down, gravity-fed, solar thermochemical receiver/reactor for direct solid particle decomposition: Design, modeling, and experimentation,” International Journal of Hydrogen Energy, Vol. 37, No. 22, Nov. 2012, pp. 16871–16887. doi: 10.1016/j.ijhydene.2012.08.086.

[33] Weiss, R. J., Ly, H. C., Wegner, K., Pratsinis, S. E., and Steinfeld, A., “H2 production by Zn hydrolysis in a hot-wall aerosol reactor,” AIChE Journal, Vol. 51, No. 7, Jul. 2005, pp. 1966–1970. doi: 10.1002/aic.10437.

[34] Wegner, K., Ly, H. C., Weiss, R. J., Pratsinis, S. E., and Steinfeld, A., “In situ formation and hydrolysis of Zn nanoparticles for H2 production by the 2-step ZnO/Zn water-splitting thermochemical cycle,” International Journal of Hydrogen Energy, Vol. 31, No. 1, Jan. 2006, pp. 55–61. doi: 10.1016/j.ijhydene.2005.03.006.

[35] Ernst, F. O., Tricoli, A., Pratsinis, S. E., and Steinfeld, A., “Co-synthesis of H2 and ZnO by In-Situ Zn Aerosol Formation and Hydrolysis,” AIChE Journal, Vol. 52, No. 9, 2006, pp. 3297–3303. doi: 10.1002/aic.10915.

[36] Hamed, T. A., Davidson, J. H., and Stolzenburg, M., “Hydrolysis of evaporated Zn in a hot wall flow reactor,” Journal of Solar Energy Engineering, Vol. 130, No. 4, 2008, p. 041010–1/7. doi: 10.1115/1.2969808.

[37] Melchior, T., Piatkowski, N., and Steinfeld, A., “H2 production by steam-quenching of Zn vapor in a hot-wall aerosol flow reactor,” Chemical Engineering Science, Vol. 64, No. 5, Mar. 2009, pp. 1095–1101. doi: 10.1016/j.ces.2008.11.002.

[38] Loutzenhiser, P. G., Gálvez, M. E., Hischier, I., Graf, A., and Steinfeld, A., “CO2 splitting in an aerosol flow reactor via the two-step Zn/ZnO solar thermochemical cycle,” Chemical Engineering Science, Vol. 65, No. 5, Mar. 2010, pp. 1855–1864. doi: 10.1016/j.ces.2009.11.025.

[39] Funke, H. H., Diaz, H., Liang, X., Carney, C. S., Weimer, A. W., and Li, P., “Hydrogen generation by hydrolysis of zinc powder aerosol,” International Journal of Hydrogen Energy, Vol. 33, No. 4, Feb. 2008, pp. 1127–1134. doi: 10.1016/j.ijhydene.2007.12.061.

[40] Loutzenhiser, P. G., Barthel, F., Stamatiou, A., and Steinfeld, A., “CO2 reduction with Zn particles in a packed-bed reactor,” AIChE Journal, Vol. 57, No. 9, 2011, pp. 2529–2534. doi: 10.1002/aic.12460.

[41] Stamatiou, A., Loutzenhiser, P. G., and Steinfeld, A., “Syngas Production from H2O and CO2 over Zn Particles in a Packed-bed Reactor,” AIChE Journal, Vol. 58, No. 2, 2012, pp. 625–631. doi: 10.1002/aic.12580.

[42] Ermanoski, I., Siegel, N. P., and Stechel, E. B., “A new reactor concept for efficient solar-thermochemical fuel production,” Journal of Solar Energy Engineering, Vol. 135, No. 3, Feb. 2013, p. 031002–1/10. doi: 10.1115/1.4023356.

[43] Scheffe, J. R., Welte, M., and Steinfeld, A., “Thermal Reduction of Ceria within an Aerosol Reactor for H2O and CO2 Splitting,” Industrial & Engineering Chemistry Research, Vol. 53, No. 6, Feb. 2014, pp. 2175–2182. doi: 10.1021/ie402620k.

[44] Steinfeld, A., and Kuhn, P., “High-temperature solar thermochemistry: production of iron and synthesis gas by Fe3O4-reduction with methane,” Energy, Vol. 18, No. 3, 1993, pp. 239–249. doi: 10.1016/0360-5442(93)90108-p.

[45] von Zedtwitz, P., and Steinfeld, A., “Steam-Gasification of Coal in a Fluidized-Bed/Packed-Bed Reactor Exposed to Concentrated Thermal Radiation - Modeling and Experimental Validation,” Industrial & Engineering Chemistry, Vol. 44, No. 11, 2005, pp. 3852–3861. doi: 10.1021/ie050138w.

[46] von Zedtwitz, P., Lipiński, W., and Steinfeld, A., “Numerical and experimental study of gas–particle radiative heat exchange in a fluidized-bed reactor for steam-gasification of coal,” Chemical Engineering Science, Vol. 62, No. 1–2, Jan. 2007, pp. 599–607. doi: 10.1016/j.ces.2006.09.027.

[47] Z’Graggen, A., Haueter, P., Trommer, D., Romero, M., de Jesus, J. C., and Steinfeld, A., “Hydrogen production by steam-gasification of petroleum coke using concentrated solar power—II Reactor design, testing, and modeling,” International Journal of Hydrogen Energy, Vol. 31, No. 6, May 2006, pp. 797–811. doi: 10.1016/j.ijhydene.2005.06.011.

[48] Melchior, T., Perkins, C., Lichty, P., Weimer, A. W., and Steinfeld, A., “Solar-driven biochar gasification in a particle-flow reactor,” Chemical Engineering and Processing, Vol. 48, No. 8, Aug. 2009, pp. 1279–1287. doi: 10.1016/j.cep.2009.05.006.

[49] Maag, G., and Steinfeld, A., “Design of a 10 MW Particle-Flow Reactor for Syngas Production by Steam-Gasification of Carbonaceous Feedstock Using Concentrated Solar Energy,” Energy & Fuels, Vol. 24, No. 12, Dec. 2010, pp. 6540–6547. doi: 10.1021/ef100936j.

[50] Kruesi, M., Jovanovic, Z. R., and Steinfeld, A., “A two-zone solar-driven gasifier concept: Reactor design and experimental evaluation with bagasse particles,” Fuel, Vol. 117, No. A, Jan. 2014, pp. 680–687. doi: 10.1016/j.fuel.2013.09.011.

[51] Nikulshina, V., Gebald, C., and Steinfeld, A., “CO2 capture from atmospheric air via consecutive CaO-carbonation and CaCO3-calcination cycles in a fluidized-bed solar reactor,” Chemical Engineering Journal, Vol. 146, No. 2, Feb. 2009, pp. 244–248. doi: 10.1016/j.cej.2008.06.005.

[52] Nikulshina, V., Halmann, M., and Steinfeld, A., “Coproduction of Syngas and Lime by Combined CaCO3-Calcination and CH4-Reforming Using a Particle-Flow Reactor Driven by Concentrated Solar Radiation,” Energy & Fuels, Vol. 23, No. 12, Dec. 2009, pp. 6207–6212. doi: 10.1021/ef9007246.

[53] Francis, T. M., Lichty, P. R., and Weimer, A. W., “Manganese oxide dissociation kinetics for the Mn2O3 thermochemical water-splitting cycle. Part 1: Experimental,” Chemical Engineering Science, Vol. 65, No. 12, Jun. 2010, pp. 3709–3717. doi: 10.1016/j.ces.2010.03.002.

[54] Dombrovsky, L.A., Lipiński, W., and Steinfeld, A, "A diffusion-based approximate model for radiation heat transfer in a solar thermochemical reactor," Journal of Quantitative Spectroscopy and Radiative Transfer, Vol. 103, pp. 601–610, 2007.

[55] Dombrovsky, A., and Lipiński, W., "A combined P_1 and Monte Carlo model for multi-dimensional radiative transfer problems in scattering media", Computational Thermal Sciences, Vol. 2, 549–560, 2010.

[56] Hathaway, B.J., Davidson, J.H., and Lipiński, W., "Heat transfer in a solar cavity receiver—design considerations", Numerical Heat Transfer Part A—Applications, Vol. 62, 445–461, 2012.

[57] Lapp, J., and Lipiński, W., "Transient three-dimensional heat transfer model of a solar thermochemical reactor for H_2O and CO_2 splitting via nonstoichiometric ceria redox cycling", Journal of Solar Energy Engineering, Vol. 136, 031006, 2014.

[58] Bala Chandran, R., Bader, R., and Lipiński, W., "Transient heat and mass transfer analysis in a porous ceria structure of a novel solar redox reactor", International Journal of Thermal Sciences, Vol. 92, 138–149, 2015.

[59] Reich, L., Bader, R., Simon, T., and Lipiński, W., "Thermal transport model of a packed-bed reactor for solar thermochemical CO_2 capture", Special Topics & Reviews in Porous Media, Vol. 6, 197–209, 2015.

[60] Wheeler, V.M., Bader, R., Kreider, P.B., Hangi, M., Haussener, S., and Lipiński, W., "Modelling of solar thermochemical reaction systems". Solar Energy, Vol. 156, 149–168, 2017.

[61] Lipiński, W., and Steinfeld, A., “Heterogeneous thermochemical decomposition under direct irradiation,” International Journal of Heat and Mass Transfer, Vol. 47, No. 8–9, Apr. 2004, pp. 1907–1916. doi: 10.1016/j.ijheatmasstransfer.2003.10.010.

[62] Lipiński, W., and Steinfeld, A., “Transient radiative heat transfer within a suspension of coal particles undergoing steam gasification,” Heat and Mass Transfer, Vol. 41, No. 11, Jul. 2005, pp. 1021–1032. doi: 10.1007/s00231-005-0654-5.

[63] Lipiński, W., Z'Graggen, A., and Steinfeld, A., "Transient Radiation Heat Transfer Within a Nongray Nonisothermal Absorbing-Emitting-Scattering Suspension of Reacting Particles Undergoing Shrinkage," Numerical Heat Transfer, Part B: Fundamentals, Vol. 47, No. 5, Apr. 2005, pp. 443–457. doi: 10.1080/10407790590928955.

[64] Lipiński, W., Thommen, D., and Steinfeld, A., "Unsteady radiative heat transfer within a suspension of ZnO particles undergoing thermal dissociation," Chemical Engineering Science, Vol. 61, No. 21, Nov. 2006, pp. 7029–7035. doi: 10.1016/j.ces.2006.07.037.

[65] Z'Graggen, A., and Steinfeld, A., "A two-phase reactor model for the steam-gasification of carbonaceous materials under concentrated thermal radiation," Chemical Engineering and Processing, Vol. 47, No. 4, Apr. 2008, pp. 655–662. doi: 10.1016/j.cep.2006.12.003.

[66] Z'Graggen, A., and Steinfeld, A., "Heat and mass transfer analysis of a suspension of reacting particles subjected to concentrated solar radiation – Application to the steam-gasification of carbonaceous materials," International Journal of Heat and Mass Transfer, Vol. 52, No. 1–2, Jan. 2009, pp. 385–395. doi: 10.1016/j.ijheatmasstransfer.2008.05.023.

[67] Schunk, L. O., Lipiński, W., and Steinfeld, A., "Ablative heat transfer in a shrinking packed bed of ZnO undergoing solar thermal dissociation," AIChE Journal, Vol. 55, No. 7, 2009, pp. 1659–1666. doi: 10.1002/aic.11782.

[68] Perkins, C., and Weimer, A., "Computational Fluid Dynamics Simulation of a Tubular Aerosol Reactor for Solar Thermal ZnO Decomposition," Journal of Solar Energy Engineering, Vol. 129, No. 4, 2007, pp. 391–404. doi: 10.1115/1.2769700.

[69] Haussener, S., Hirsch, D., Perkins, C., Weimer, A., Lewandowski, A., and Steinfeld, A., "Modeling of a Multitube High-Temperature Solar Thermochemical Reactor for Hydrogen Production," Journal of Solar Energy Engineering, Vol. 131, No. 2, 2009, p. 024503–1/5. doi: 10.1115/1.3097280.

[70] Melchior, T., Perkins, C., Weimer, A. W., and Steinfeld, A., "A cavity-receiver containing a tubular absorber for high-temperature thermochemical processing using concentrated solar energy," International Journal of Thermal Sciences, Vol. 47, No. 11, Nov. 2008, pp. 1496–1503. doi: 10.1016/j.ijthermalsci.2007.12.003.

[71] Martinek, J., Bingham, C., and Weimer, A. W., “Computational modeling and on-sun model validation for a multiple tube solar reactor with specularly reflective cavity walls. Part 1: Heat transfer model,” Chemical Engineering Science, Vol. 81, Oct. 2012, pp. 298–310. doi: 10.1016/j.ces.2012.06.064.

[72] Babiniec, S. M., Coker, E. N., Miller, J. E., and Ambrosini, A., “Investigation of LaxSr1-xCoyM1-yO3-d (M = Mn, Fe) perovskite materials as thermochemical energy storage media,” Solar Energy, Vol. 118, 2015, pp. 451–459. doi: 10.1016/j.solener.2015.05.040.

[73] Imponenti, L., Albrecht, K. J., Wands, J. W., Sanders, M. D., and Jackson, G. S., “Thermochemical energy storage in strontium-doped calcium manganites for concentrating solar power applications,” Solar Energy, Vol. 151, 2017, pp. 1–13. doi: 10.1016/j.solener.2017.05.010.

[74] Bush, H. E., Schlichting, K.-P., Gill, R. J., Jeter, S. M., and Loutzenhiser, P. G., “Design and Characterization of a Novel Upward Flow Reactor for the Study of High-Temperature Thermal Reduction for Solar-Driven Processes,” Journal of Solar Energy Engineering, Vol. 139, No. 5, 2017, p. 51004. doi: 10.1115/1.4037191.

[75] Gobereit, B., Amsbeck, L., Buck, R., Pitz-Paal, R., Röger, M., and Müller-Steinhagen, H., “Assessment of a falling solid particle receiver with numerical simulation,” Solar Energy, Vol. 115, 2015, pp. 505–517. doi: 10.1016/j.solener.2015.03.013.

[76] Keene, D. J., Davidson, J. H., and Lipiński, W., “A model of transient heat and mass transfer in a heterogeneous medium of ceria undergoing nonstoichiometric reduction,” Journal of Heat Transfer, Vol. 135, No. 5, 2013, p. 052701–1/9. doi: 10.1115/1.4023494.

[77] Modest, M. F., *Radiative Heat Transfer*, Amsterdam: Academic Press, 2013.

[78] Bohren, C. F., and Huffman, D. R., *Absorption and Scattering of Light by Small Particles*, New York: John Wiley & Sons, 1983.

[79] Dombrovsky, L. A., and Baillis, D., *Thermal Radiation Disperse Systems: An Engineering Approach*, New York: Begell House, Inc., 2010.

[80] Kunii, D., and Levenspiel, O., *Fluidization Engineering*, Newton, MA: Butterworth-Heinemann, 1991.

[81] Panlener, R. J., Blumenthal, R. N., and Garnier, J. E., “A thermodynamic study of nonstoichiometric cerium dioxide,” Journal of Physics and Chemistry of Solids, Vol. 36, No. 11, 1975, pp. 1213–1222. doi:

10.1016/0022-3697(75)90192-4.

[82] Liang, Z., Chueh, W. C., Ganesan, K., Haile, S. M., and Lipiński, W., "Experimental determination of transmittance of porous cerium dioxide media in the spectral range of 300–1,100 nm," Experimental Heat Transfer, Vol. 24, 2011, pp. 285–299. doi: 10.1080/08916152.2010.542876.

[83] Ganesan, K., and Lipiński, W., "Experimental Determination of Spectral Transmittance of Porous Cerium Dioxide in the Range 900–1700 nm," Journal of Heat Transfer, Vol. 133, No. 10, 2011, p. 104501. doi: 10.1115/1.4003970.

[84] Dombrovsky, L., Ganesan, K., and Lipiński, W., "Combined two-flux approximation and Monte Carlo model for identification of radiative properties of highly scattering dispersed materials," Computational Thermal Sciences, Vol. 4, No. 4, 2012, pp. 365–378. doi: 10.1615/ComputThermalScien.2012005025.

[85] Ganesan, K., Dombrovsky, L. A., and Lipiński, W., "Visible and near-infrared optical properties of ceria ceramics," Infrared Physics & Technology, Vol. 57, 2013, pp. 101–109. doi: 10.1016/j.infrared.2012.12.040.

[86] Ganesan, K., Dombrovsky, L. A., Oh, T.-S., and Lipiński, W., "Determination of optical constants of ceria by combined analytical and experimental approaches," The Journal of Minerals, Metals & Materials Society (JOM), Vol. 65, No. 12, 2013, pp. 1694–1701. doi: 10.1007/s11837-013-0708-y.

[87] Patsalas, P., Logothetidis, S., and Metaxa, C., "Optical performance of nanocrystalline transparent ceria films," Applied Physics Letters, Vol. 81, No. 3, 2002, pp. 466–468. doi: 10.1063/1.1494458.

[88] Marabelli, F., and Wachter, P., "Covalent insulator CeO2: optical reflectivity measurements," Physical Review B, Condensed Matter, Vol. 36, No. 2, 1987, pp. 1238–1243. doi: 10.1103/physrevb.36.1238.

[89] Sun, L.-L., Cheng, Y., and Ji, G.-F., "Elastic and optical properties of CeO2 via first-principles calculations," Journal of Atomic and Molecular Sciences, Vol. 1, No. 2, 2010, pp. 143–151. doi: 10.4208/jams.081109.091809a.

[90] Binnewies, M., and Milke, E., *Thermochemical Data of Elements and Compounds*, Weinheim: Wiley-VCH Verlag GmbH, 2002.

[91] Shampine, L., and Gordon, M., *Computer Solution of Ordinary Differential Equations: The Initial Value Problem*, 1975.

[92] Shampine, L. ., and Gordon, M. K., “ode.f90”

[93] Howell, J. R., Mengüç, M. P., and Siegel, R., *Thermal Radiation Heat Transfer*, New York: Taylor & Francis, 2015.

[94] Dombrovsky, L. A., “The Use of Transport Approximation and Diffusion-Based Models in Radiative Transfer Calculations,” Computational Thermal Sciences, Vol. 4, No. 4, 2012, pp. 297–315. doi: 10.1615/ComputThermalScien.2012005050.